

1 Processing Multiple GNSS RO Data Using FSI and ROPP: Results from the ROMEX

2
3 Yong Chen¹, Xinjia Zhou², Xin Jing³, Shu-Peng Ho¹, Xi Shao³, and Tung-Chang Liu³

4 ¹NOAA/NESDIS/STAR, College Park, MD, 20740, USA

5 ²ERT, Laurel, MD, 20707, USA

6 ³CISESS/ESSIC, University of Maryland, College Park, MD, 20740, USA

7 Corresponding to: Yong Chen (Yong.Chen@noaa.gov)

8 9 Abstract

10
11 Global Navigation Satellite System (GNSS) Radio Occultation (RO) is a vital technique in
12 atmospheric remote sensing, providing all-weather, high-resolution vertical observations that
13 support numerical weather prediction (NWP) and atmospheric research. To enhance
14 understanding of GNSS RO processing uncertainties and inter-algorithm consistency,
15 NOAA/STAR developed an independent RO inversion algorithm based on the Full Spectrum
16 Inversion (FSI) technique to derive bending angle and refractivity profiles from excess phase
17 data. As part of the international Radio Occultation Modeling Experiment (ROMEX), endorsed
18 by the International Radio Occultation Working Group (IROWG), STAR's FSI results were
19 systematically compared with outputs from the community standard Radio Occultation
20 Processing Package (ROPP) and EUMETSAT datasets. Leveraging multi-GNSS RO
21 observations from both commercial and government-funded missions, the study evaluates
22 consistency across processing approaches using the European Centre for Medium-Range
23 Weather Forecasts (ECMWF) Reanalysis v5 (ERA5) as the reference and structural differences
24 against the three-dataset mean for the ROMEX period. Results reveal high overall agreement,
25 while identifying variations linked to the signal-to-noise ratio (SNR) and mission
26 characteristics, providing critical insights for interpreting ROMEX forecast impact studies and
27 improving GNSS RO data assimilation systems.

28 29 1. Introduction

30
31 Global Navigation Satellite System (GNSS) Radio Occultation (RO) has become a cornerstone
32 of atmospheric remote sensing, offering high vertical resolution, global coverage, long-term
33 stability, and minimal bias (Kursinski et al., 1997; Anthes et al., 2008; Ho et al., 2020). By
34 measuring the bending of GNSS signals as they pass through the atmosphere, RO enables
35 retrievals of refractivity, temperature, pressure, and humidity profiles. As a limb-sounding
36 technique, it is largely unaffected by clouds and precipitation, providing an all-weather
37 observing capability essential for weather forecasting and climate monitoring (Cucurull et al.,
38 2007; Healy, 2008; Steiner et al., 2020).

39
40 Over the past two decades, the expansion of GNSS constellations (e.g., GPS, GLONASS,
41 Galileo, BeiDou) and the increasing availability of RO missions, including government-funded
42 programs (e.g., COSMIC-1/2, Metop-A/B/C, Sentinel-6) and commercial ventures (e.g., Spire,
43 GeoOptics, PlanetiQ), have significantly increased the volume of RO observations (Anthes,
44 2011; Schreiner et al., 2020; Ho et al., 2023). Today, global RO data counts exceed 35,000-
45 40,000 profiles per day, with substantial contributions from commercial providers through
46 initiatives such as NOAA's Commercial Data Purchase (CDP) program. While this growth
47 enhances the value of RO for numerical weather prediction (NWP) and climate applications, it
48 also introduces challenges due to differences in instrument design, tracking strategies,
49 sampling patterns, and processing methodologies.

51 RO retrievals involve several steps: i) deriving clock-synchronized excess phase and signal-to-
52 noise ratio (SNR) data, ii) inverting excess phase to bending angle (BA) profiles, and iii)
53 retrieving refractivity from BA via Abel or statistical methods (Gorbunov, 2002a). In the lower
54 troposphere, strong gradients and multipath propagation complicate retrievals, motivating
55 advanced inversion techniques such as Full Spectrum Inversion (FSI) (Jensen et al., 2003;
56 Adhikari et al., 2016, 2021), Canonical Transform Type 2 (CT2) (Gorbunov et al., 2005), and
57 Phase Matching (PM) (Jensen et al., 2004; Sokolovskiy et al., 2011). FSI relies on explicit
58 signal localization to enhance vertical resolution and mitigate multipath by reducing spectral
59 mixing, whereas CT2 achieves an implicit, physics-based localization in impact parameter
60 space, enabling more robust separation of multipath contributions. While FSI is designed to
61 leverage full-spectrum information for potentially enhanced sensitivity to fine-scale
62 atmospheric structures, it is also generally more noise-sensitive. CT2, in contrast, provides
63 more stable retrievals in strong multipath conditions, sometimes at the expense of reduced
64 small-scale resolution. Consequently, the effective vertical resolution of both methods is highly
65 dependent on specific implementation and tuning choices, such as filter settings and truncation
66 strategies.

67
68 The international RO community is currently undertaking a coordinated effort to evaluate the
69 impact of large volumes of RO data on NWP. This initiative, known as the Radio Occultation
70 Modeling Experiment (ROMEX), is endorsed by the International Radio Occultation Working
71 Group (IROWG) (<https://irowg.org/ro-modeling-experiment-romex/>) and provides a
72 collaborative platform for data providers and processing centers to assess RO retrievals under
73 a standardized framework (Anthes et al., 2024). GNSS RO observations from a broad range of
74 government-funded and commercial missions were submitted to EUMETSAT for centralized
75 processing, and the resulting products were distributed via the Radio Occultation Meteorology
76 Satellite Application Facility (ROM SAF). ROMEX provides a standardized framework for
77 assessing inter-mission and inter-algorithm differences. Central questions include whether
78 assimilating larger RO volumes improves forecasts, and how variations in data quality and
79 inversion methods affect the outcome.

80
81 In support of ROMEX, the NOAA Center for Satellite Applications and Research (STAR)
82 contributed independent datasets processed using the FSI algorithm (RFSI), which was
83 integrated into version 10.0 of the Radio Occultation Processing Package (ROPP) (ROPP,
84 2020). This customized system, hereafter referred to as STAR ROPP, retains compliance with
85 ROPP standards while incorporating STAR-developed retrieval capability, including both the
86 CT2 and FSI methods for bending angle retrieval. Here, STAR RFSI denotes the STAR
87 implementation of the FSI-based bending angle retrieval, while STAR ROPP refers to the
88 customized ROPP v10.0 framework developed at STAR that supports both CT2 and FSI
89 processing. This system is distinct from the official ROM SAF ROPP, which serves as the
90 community standard. In this study, the community-standard dataset refers specifically to data
91 generated using the STAR ROPP CT2 method. Maintaining this distinction is essential, as it
92 enables an independent assessment of algorithmic effects on RO data quality.

93
94 FSI offers a specific approach for resolving fine-scale atmospheric structures and handling
95 multipath in the lower troposphere (Jensen et al., 2003; Adhikari et al., 2021), a key source of
96 uncertainty for NWP. The use of the STAR RFSI algorithm within ROMEX is therefore to
97 quantify the structural uncertainty associated with this alternative retrieval approach, which is
98 sensitive to small-scale features, relative to community-standard methods, thereby providing
99 critical insight for optimizing multi-mission data assimilation strategies.

100

101 This study evaluates the STAR FSI-based processing system within the ROMEX framework.
102 Retrievals from RFSI are compared against those from the STAR ROPP with the CT2 method
103 and the EUMETSAT-processed ROMEX dataset (with COSMIC-2 data provided by UCAR).
104 The analysis focuses on November 2022 and utilizes the European Centre for Medium-Range
105 Weather Forecasts (ECMWF) Reanalysis v5 (ERA5) (Hersbach et al., 2023) as a reference to
106 evaluate algorithmic performance across various missions. The STAR RFSI dataset for
107 ROMEX is one of the three RO datasets, along with those from EUMETSAT and UCAR, that
108 were released to ROMEX participants through ROM-SAF (Shao and Folsche, 2024).

109

110 Intercomparisons included statistical evaluations (mean biases, standard deviations) and inter-
111 algorithm consistency. This design helps isolate processing-related uncertainties (e.g.,
112 structural uncertainty; Ho et al., 2012) and ensures that differences in NWP impact can be
113 attributed to data quality and processing methodology rather than uncontrolled input or
114 evaluation effects.

115

116 The paper is organized as follows: Section 2 describes the GNSS RO observations and datasets
117 used in this study. Section 3 presents the FSI algorithm in detail. Section 4 provides inter-
118 algorithm and inter-mission comparison results using ROMEX RO data. Conclusions are
119 summarized in section 5.

120

121 **2. GNSS RO Observations and Data Used in this Study**

122 **2.1 GNSS RO Observations**

123

124 Modern satellite missions, including COSMIC-2, Spire, and PlanetiQ, have significantly
125 increased the volume of GNSS radio occultation data. These missions track signals from
126 multiple constellations, including GPS, GLONASS, Galileo, and BeiDou, thereby improving
127 global spatial and temporal coverage for atmospheric profiling.

128

129 LEO satellite receivers track GNSS signals using two primary methods: Closed Loop (CL) and
130 Open Loop (OL). CL tracking ensures stable signal acquisition in the upper atmosphere but
131 may fail under rapidly varying conditions in the lower troposphere. OL tracking, by contrast,
132 is specifically designed to capture multipath-affected signals in the lower atmosphere. The
133 combination use of CL and OL tracking was traditionally adopted to ensure reliable
134 performance across the full vertical extent of the atmosphere. However, recent GNSS radio
135 occultation missions, including COSMIC-2, Spire, and PlanetiQ, primarily employ OL
136 tracking throughout the occultation in order to maximize tracking robustness and data
137 continuity across all atmospheric layers.

138

139 The raw data, consisting of signal phase and amplitude measurements, are processed to
140 calculate bending angle and refractivity profiles. A critical step in this process is correcting
141 ionospheric effects. This is achieved by using dual-frequency signals (e.g., L1 and L2), which
142 allow separation of the frequency-dependent ionospheric interference from the non-dispersive
143 signal of the neutral atmosphere. This isolation is essential for accurate atmospheric retrievals.

144

145 **2.2 RO Data Used in this Study**

146

147 This study utilizes Level 1b atmospheric excess phase data (in conPhs/atmPhs format) from
148 the ROMEX campaign. The dataset includes contributions from commercial providers, such
149 as PlanetiQ, Spire, and GeoOptics, as well as government-funded missions, including Metop-
150 B/C and COSMIC-2. A summary of mission-specific data coverage for the period 1 September

151 to 30 November 2022 is provided in Table 1. These excess phase datasets, delivered in NetCDF
 152 format and available exclusively to ROMEX participants, serve as the primary input for
 153 deriving neutral atmospheric bending angle and refractivity profiles. On average, the dataset
 154 comprises approximately 37,900 profiles per day.

155
 156 The high scientific value and cost-effectiveness of GNSS RO technology have driven increased
 157 private-sector participation in recent years. U.S. companies Spire Global, PlanetiQ, and
 158 GeoOptics, along with Yunyao Aerospace in China, have deployed RO receivers on
 159 commercial satellites to supply high-quality data to the scientific community. Among them,
 160 Spire Global Inc. contributes approximately 17,000 profiles per day to ROMEX, followed by
 161 Yunyao Aerospace with about 6,200, PlanetiQ with about 3,300, and GeoOptics with roughly
 162 300.

163
 164 Several government-funded RO satellite missions were routinely processed by the UCAR
 165 COSMIC Data Analysis and Archive Center (CDAAC) and made available to both the research
 166 and operational communities during the ROMEX period. These missions include COSMIC-2
 167 (~6,000 profiles/day), KOMPSAT-5 (~300), PAZ (~200), and both TerraSAR-X and
 168 TanDEM-X (~100 each). RO data from Metop-B/C and Sentinel-6 were provided by
 169 EUMETSAT, delivering approximately 1,200 and 800 profiles per day, respectively. RO
 170 profiles from FY-3C/D/E and Tianmu were supplied by the National Satellite Meteorological
 171 Center (NSMC) of the Chinese Meteorological Administration (CMA) and the National Space
 172 Science Center (NSSC) of the Chinese Academy of Sciences (CAS), respectively, with average
 173 daily counts of approximately 2,100 and 300.

174
 175 For this study, we processed RO data from all ROMEX missions except Sentinel-6 and
 176 GeoOptics, as well as from the Chinese government or Chinese companies (e.g., FY-3,
 177 Yunyao, and Tianmu). For each processed mission, we generated bending angle and
 178 refractivity profiles using both the STAR RFSI and STAR ROPP (CT2) algorithms. These
 179 datasets were submitted to EUMETSAT and distributed to ROMEX participants through the
 180 ROM SAF. By processing multiple missions with independent algorithms, we ensured
 181 consistent inputs across platforms. We enabled a direct assessment of algorithm-dependent
 182 uncertainties, thereby clarifying how data processing influences the interpretation of ROMEX
 183 NWP impact experiments. Table 2 summarizes the typical SNR characteristics of GNSS
 184 receivers across different missions, supporting the discussion of mission-dependent
 185 performance and structural uncertainties.

186
 187 Table 1: RO Missions are included in ROMEX
 188

RO mission	RO profiles/day	Excess provider	phase STAR ROPP/RFSI	EUMETSAT
Metop B, C (GRAS)	1200	EUMETSAT	√	√
COSMIC-2	6000	UCAR	√	√ [#]
SPIRE	17000	Spire	√	√ [*]
PlanetiQ	3300	PlanetiQ	√	√ [*]
GeoOptics	300	GeoOptics	x	√
KOMPSAT-5	300	UCAR	√	√
PAZ	200	UCAR	√	√
TerraSAR-X	100	UCAR	√	√
TanDEM-X	100	UCAR	√	√

Sentinel-6	800	EUMETSAT	x	√
FY3-C, D, E (GNOS)	2100	CMA/NSMC	x	√
Yun Yao	6200	Yun Yao	x	√
Tianmu	300	CAS/NSSC	x	√
ROMEX total	37900			

189 √[#] UCAR provided both bending angle and refractivity in the EUMETSAT ROMEX dataset.
 190 √* No refractivity available in the EUMETSAT dataset for PlanetiQ and Spire, only bending
 191 angle
 192

193 Table 2 Signal-to-Noise Ratio (SNR)[#] characteristics of GNSS receivers across different
 194 missions

RO mission	GPS	GLONASS	Galileo	BeiDou
Metop B	730.2			
Metop C	789.3			
COSMIC-2	1295.1	1181.4		
SPIRE	387.9	707.2	316.4	
PlanetiQ	1440.5	1580.6	1124.8	1335.7
KOMPSAT-5	617.2			
PAZ	503.9			
TerraSAR-X	622.4			
TanDEM-X	549.3			

195 [#] Mean SNR between altitudes 60 km and 80 km, with unit (volt/volt)
 196

197 3. Full Spectrum Inversion Algorithm and Processing Chain

198
 199 The core FSI algorithm remains consistent with that described in Adhikari et al. (2021). The
 200 novelty of the present work is not in the invention of the FSI algorithm, but in the
 201 successful development and systematic application of the complete STAR RFSI end-to-end
 202 processing framework and its subsequent inclusion in the ROMEX intercomparison as an
 203 independent data source.
 204

205 The scientific contribution is distinct from previous FSI work in three key ways. (1) Systematic
 206 Multi-Mission Application: This study provides the first comprehensive, cross-mission
 207 validation of the STAR RFSI system using a large and diverse ROMEX dataset (including
 208 commercial and government-funded missions) against other major community processing
 209 centers (such as EUMETSAT and UCAR). (2) Quantification of Structural Uncertainty: The
 210 primary objective and scientific value of this study is the quantification of the structural
 211 uncertainty among different processing approaches, FSI, STAR CT2, and the EUMETSAT
 212 ROM SAF ROPP CT2, under a ROMEX framework. This analysis provides critical metrics
 213 for interpreting ROMEX forecast impact studies. (3) Operational Documentation: The
 214 manuscript documents the complete STAR RFSI processing chain (including data
 215 preprocessing, quality control, and statistical optimization), which is essential for transparency
 216 and future operational use within NOAA STAR. The STAR RFSI algorithm provides a robust
 217 framework for generating bending-angle and refractivity profiles from GNSS RO
 218 measurements, particularly in the presence of lower-tropospheric multipath. As described by
 219 Chen et al. (2024), the STAR RFSI algorithm has been integrated into ROPP version 10.0
 220 customized at NOAA STAR. RFSI processes dual-frequency excess phase and SNR data along

221 with satellite position and timing information. It supports a wide range of satellite missions and
 222 tracking configurations.

223

224 The STAR RFSI end-to-end process involves four main steps (see Fig. 1):

225

226 (1) data input and pre-processing: RO data, including satellite geometry, excess phase, and
 227 SNR measurements, are ingested and prepared for further processing. Satellite coordinates, if
 228 provided at lower frequencies, are interpolated to align with the sampling time using clock
 229 bias-corrected transmitter and receiver times (see Section 3.1).

230

231 (2) bending angle calculation: excess phase data are converted to bending angles, with
 232 ionospheric corrections applied using dual-frequency measurements (see Section 3.2).

233

234 (3) inversion to refractivity and dry temperature: bending angles are inverted using Abel
 235 integration to derive refractivity profiles, which can subsequently be used to compute dry
 236 atmospheric temperature (see Section 3.3).

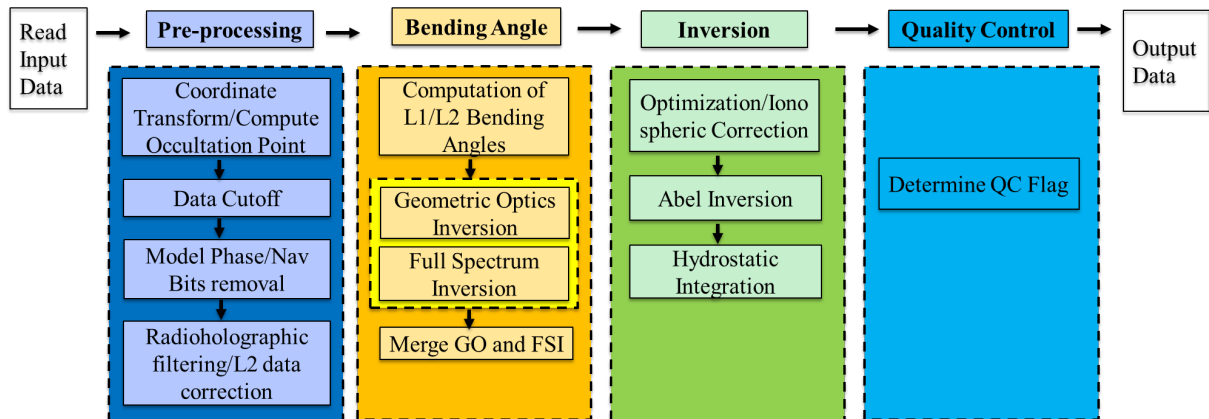
237

238 (4) quality control (QC): a comprehensive quality assessment is conducted by applying quality
 239 flags based on threshold criteria for bending angle differences, determined through
 240 comparisons with ERA5 simulations. This process ensures that only high-quality profiles are
 241 retained as valid (see Section 3.4). Additionally, we have developed an internal quality control
 242 system designed explicitly for near-real-time processing. This internal check was not included
 243 in the ROMEX data when it was generated.

244

245 Figure 1 illustrates the complete RO data processing workflow implemented in the STAR FSI
 246 system, highlighting the transition from raw signal acquisition to the generation of quality-
 247 controlled atmospheric profiles (bending angle and refractivity).

248



249

250

251 Fig. 1: Flow chart depicting the steps used in the FSI RO data processing of the geometry and
 252 phase data.

253

254 3.1 Data Input and Pre-processing

255

256 The STAR RFSI system ingests Level 1b dual-frequency excess phase and SNR data, along
 257 with satellite position and time information, to generate high-resolution atmospheric profiles.
 258 The geometry files typically contain satellite position vectors at a lower sampling rate (e.g., 1
 259 Hz), whereas the excess phase and SNR are sampled at higher rates (e.g., 50-100 Hz). To align

260 these data, satellite coordinates are interpolated to the excess-phase sampling times using
 261 clock-bias-corrected receiver and transmitter times. Satellite geometry and excess phase/SNR
 262 time series are interpolated into a common sampling rate. Given start time (t_s), sampling time
 263 (t), and clock bias-corrected receiver time (t_{orb}) and transmitter time (t_{txm}), the interpolated
 264 receiver coordinates (r_{leo}), transmitter time (t_{txmHR}), and GNSS coordinates (r_{gns}) can be
 265 calculated using cubic spline interpolation as:

$$266 \quad r_{leo} = \text{interpolate}(r_{leoLR}, t_{orb}, t + t_s, /cubic_spline) \quad (1)$$

$$267 \quad t_{txmHR} = \text{interpolate}(t_{txm}, t_{orb}, t + t_s) \quad (2)$$

$$268 \quad r_{gns} = \text{interpolate}(r_{gnsLR}, t_{txm}, t_{txmHR}, /cubic_spline) \quad (3)$$

269 where r_{leoLR} and r_{gnsLR} are the original coordinates.

270
 271 The time series of satellite positions is initially provided in the Earth-Centered Inertial (ECI)
 272 J2000 frame. These positions are converted to Earth-Centered Earth-Fixed (ECEF) coordinates
 273 according to the IERS 2010 conventions, which include corrections for polar motion and Earth
 274 rotation (Adhikari et al., 2021; Petit and Luzum, 2010; Luzum and Petit, 2010). This
 275 transformation enables geolocation of the occultation tangent point at each time step.

276
 277 To satisfy the assumption of local spherical symmetry during inversion, occultation geometry
 278 is reprojected to the local center of curvature. The tangent point location on the reference
 279 ellipsoid (WGS84) is determined where the straight line between the transmitter and receiver
 280 touches the ellipsoid. The latitude, longitude, local radius of curvature, and the center of
 281 curvature are computed at this reference tangent point and used to shift both GNSS and LEO
 282 positions into a local spherical coordinate system. This step ensures accurate mapping of
 283 impact parameters and tangent altitudes for each ray path.

284
 285 RO signals acquired using OL tracking may contain low-SNR regions near the surface due to
 286 signal fading or tracking loss (see Figure 5 in Adhikari et al., 2021). An appropriate cut-off
 287 height is essential to ensure the accuracy and reliability of tropospheric information retrieved
 288 from GNSS signals in OL tracking mode (Sokolovskiy et al., 2009; Sokolovskiy et al., 2010;
 289 Adhikari et al., 2021; Paoletta et al., 2025). To prevent the propagation of noise-contaminated
 290 signals through the inversion chain, a systematic signal truncation method is employed using
 291 SNR-based thresholds in this study. The truncation procedure includes the following steps: (1)
 292 initial cut-off impact height: the initial threshold of impact height is set based on the LEO
 293 satellite's altitude, as it influences the signal's penetration depth and the quality of retrieved
 294 atmospheric profiles; (2) dynamic background SNR calculation: the background SNR is
 295 estimated for each time series using the lowest 10 seconds of the smoothed data. A 3-second
 296 moving average is applied to the time series to smooth out high-frequency fluctuations; (3)
 297 initial SNR threshold determination: starting from the lowest point in the time series, the first
 298 point where the SNR exceeds three times the calculated background SNR in step (2) is
 299 identified as a preliminary threshold. (4) final cut-off point selection: moving backward from
 300 the uppermost point identified in step (3), the cut-off point is determined as the first point where
 301 the SNR drops below 1.5 times the background SNR, and the associated impact height is higher
 302 than the threshold established in step (1).

303
 304 This filtering removes anomalous low-level SNR spikes, which can occur due to OL tracking
 305 artifacts, particularly in tropical and high-humidity conditions. Improper truncation can
 306

310 degrade the quality of bending angle measurements: truncating too high removes real signals,
 311 introducing a negative bias, while truncating too low retains noise, leading to oscillations in
 312 the retrieved profiles. The chosen thresholds aim to maximize vertical coverage without
 313 sacrificing data quality.

314

315 **3.2 Computation of Bending Angles using Full Spectrum Inversion**

316

317 Bending angle retrieval is performed in two steps: (1) computation of the model phase and
 318 correction of navigation bit jumps, and (2) inversion of observed signals using FSI to retrieve
 319 bending angles as a function of impact parameter.

320

321 **3.2.1 Calculation of model phase**

322

323 The model phase is derived from a reference refractivity profile computed using the MSIS-90
 324 climatology (Hedin, 1991), assuming 90% relative humidity below 15 km. Refractivity (N) is
 325 calculated as

326

$$327 \quad N = 77.6 \frac{P}{T} + 3.73 \times 10^5 \frac{e}{T^2} \quad (4)$$

328

329 where P is pressure, T is temperature, and e is water vapor. The model impact parameter (a) at
 330 altitude z is calculated as

331

$$332 \quad a = n(R + z) = nr, \quad (5)$$

333

334 where, $n = 1 + N \times 10^{-6}$, R is the local radius of curvature of the Earth, and $r = R + z$.

335

336 The bending angle (α) profile is derived from n and a using Abel integration

337

$$338 \quad \alpha(p) = 2p \int_{r_1}^{\infty} \frac{a}{\sqrt{n^2 r^2 - a^2}} \frac{d \ln(n)}{dr} dr, \quad (6)$$

339

340 The impact parameter and bending angle profiles, along with occultation time (t), satellite
 341 positions, and velocities, are then used to derive the Doppler shift associated with the
 342 atmospheric refractivity $n(z)$. The model phase, computed from occultation time and the
 343 Doppler shift, provides a reference for identifying navigation bit jumps.

344

345 In most RO data, navigation bits embedded in the excess phase and coordinate time series can
 346 introduce discontinuities of $\pm\pi$. These phase jumps are identified by comparing the measured
 347 excess phase with the model phase, especially at high sampling rates (≥ 50 Hz). Once detected,
 348 the navigation bit pattern is applied to correct discontinuities in the measured phase, ensuring
 349 continuity and accuracy in the processed phase time series. Although the MSIS model is used
 350 to calculate the reference phase for these corrections, it introduces a known source of
 351 uncertainty in the lower troposphere. This uncertainty highlights the critical need for an
 352 external navigation bit stream, since standard navigation-bit-free cycle slip correction routines
 353 (such as those in ROPP) often struggle with atmospheric multipath in this region. To mitigate
 354 this issue, processing is often terminated above a 7-10 km impact height. However, this
 355 challenge can be circumvented by using pilot signals (Galileo E1C and E5BQ, GPS L2C, and
 356 BeiDou B1CP and B2AP), which are not modulated with navigation bits and can therefore

357 yield reliable results in the lower troposphere even without external bit stream data (Jonathan
358 Brandmeyer, personal communication, June 2025).

359

360 3.2.2 Full Spectrum Inversion

361

362 To retrieve bending angles from RO signals, it is essential to reduce high-frequency noise in
363 the excess phase. This is typically achieved using low-pass or radio-holographic filters
364 (Gorbunov et al., 2005). In the current RFSI inversion system, a 0.5-second low-pass Fourier
365 filter is applied to the excess Doppler signal (the time derivative of excess phase). The filtered
366 Doppler is then reintegrated to recover a smoothed excess phase. The 0.5-second window
367 approximately matches the vertical resolution of RO observations, corresponding to the first
368 Fresnel zone (Kursinski et al., 1997). To better resolve fine-scale refractivity structures in the
369 lower atmosphere, a shorter, height-dependent smoothing window is used below 10 km: 0.05
370 seconds for 100 Hz data and 0.1 seconds for 50 Hz, enabling noise reduction while preserving
371 small-scale features. The choice of these parameters is based on systematic tuning experiments
372 in which multiple configurations were evaluated. The selected values showed here provide the
373 most consistent statistical agreement with model outputs, such as ERA5, yielding reduced
374 bending angle bias and standard deviation compared with other tested configurations.

375

376 Bending angles are computed using geometric optics (GO) above 25 km and the full spectrum
377 inversion method below this altitude. In FSI, the received signal is expressed as a sum of
378 narrowband sub-signals in the open-angle domain θ :

379

$$380 u(\theta) = \sum_p A_p(\theta) e^{i\varphi_p(\theta)} \quad (7)$$

381

382 where, A_p and φ_p are the amplitude and phase of the p th sub-signal, respectively. The Fourier
383 transform of Eq. (7) is:

384

$$385 F(\hat{\omega}) = \sum_p \int_{\theta_1}^{\theta_2} A_p(\theta') e^{i(\varphi_p - \hat{\omega}\theta')} d\theta' \quad (8)$$

386

387 where θ_1 and θ_2 represent the open angles at the start and end of the occultation, respectively.

388

389 Applying the method of stationary phase (MSP) (Born and Wolf, 1999; Jensen et al., 2003),
390 the transform simplifies to:

391

$$392 F(\hat{\omega}) \approx B e^{i(\varphi_q - \hat{\omega}_q \theta_s)} \quad (9)$$

393

394 where B is an approximately constant amplitude, and the pseudo frequency $\hat{\omega}_q$ satisfies

395

$$396 \hat{\omega}_q = \left. \frac{d\varphi_q}{d\theta} \right|_{\theta=\theta_s} \quad (10)$$

397

398 The stationary points θ_s is then given by:

399

$$400 \theta_s = -\frac{d\psi}{d\hat{\omega}}, \text{ where } \psi = \varphi_q - \hat{\omega}_q \theta_s \quad (11)$$

401

402 The derivative of the phase (φ_q) with respect to θ , accounting for the signal path from the
403 GNSS to LEO satellite, is:

404

$$\frac{d\varphi_q}{d\theta} = \hat{\omega}_q = ka + k \frac{dR_L}{d\theta} \sqrt{1 - \left(\frac{a}{R_L}\right)^2} + k \frac{dR_G}{d\theta} \sqrt{1 - \left(\frac{a}{R_G}\right)^2}, \quad (12)$$

406

407 where k is the wavenumber of the carrier signal, R_L and R_G are the distances from the GNSS
408 and LEO satellites to the local center of curvature, respectively, and a is the impact parameter.

409

410 Assuming circular orbits, the derivatives of R_L and R_G vanish, reducing Eq. (12) to:

411

$$\frac{d\varphi_q}{d\theta} = ka \quad (13)$$

413

414 Differentiating with respect to $\hat{\omega}$ gives:

415

$$da = \frac{1}{k} d\hat{\omega}, \quad (14)$$

417

418 The spectral resolution of the Fourier transform phase, $d\hat{\omega}$, is given by (Adhikari et al. 2016):

419

$$d\hat{\omega} = \frac{2\pi}{\Delta\theta}, \text{ where } \Delta\theta = \theta_2 - \theta_1 \quad (15)$$

421

422 Finally, with the impact parameter a and the open angle θ , the bending angle is computed as:

423

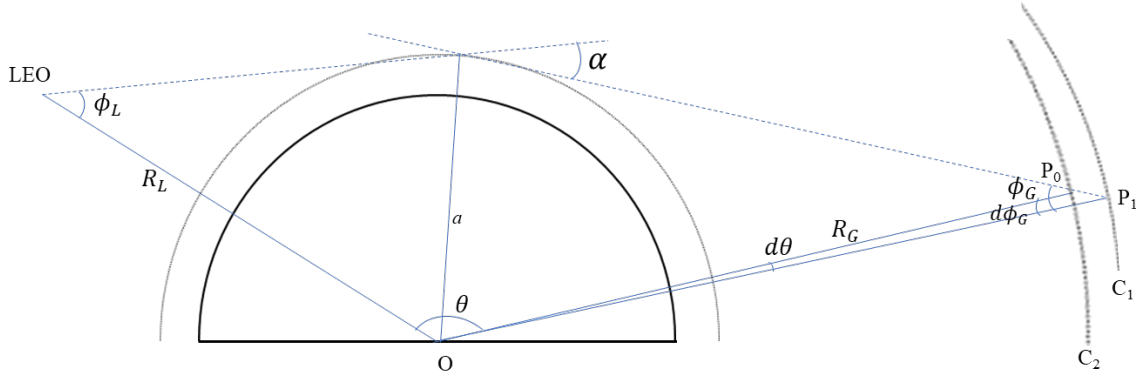
$$\alpha(a) = \theta + \arcsin\left(\frac{a}{R_L}\right) + \arcsin\left(\frac{a}{R_G}\right) - \pi. \quad (16)$$

425

426 3.2.3 Correction for non-spherical trajectory

427

428 The assumption underlying Eq. (16) is invalid in realistic occultation scenarios due to the
429 Earth's oblateness and the non-coplanar nature of GNSS and LEO satellite orbits. To account
430 for these effects, a correction must be applied to the observed phase to project the signal path
431 onto circular, coplanar trajectories. As illustrated in Fig. 2, the actual GNSS satellite orbit is
432 represented by arc C_1 , with each point along the trajectory projected onto a circular orbit, C_2 .
433 Notably, the impact parameter (a) remains unchanged during this projection. In this process,
434 the GNSS position is shifted from P_1 on arc C_1 to P_0 on arc C_2 . This projection alters the open
435 angle (θ), the signal ray (ϕ_G), and the phase of the signal. Although Fig. 2 focuses on the GNSS
436 orbit, the same projection method is also applied to the LEO receiver orbit. Given the known
437 positions of the GNSS and LEO satellites, the resulting changes in phase and open angles can
438 be determined geometrically. Note that the radius and center of curvature are treated as fixed
439 for a given RO event and are not dynamically reprojected. The projection is performed with
440 respect to the precomputed local center of curvature, ensuring a consistent coordinate system
441 throughout the inversion process.



442 Fig. 2: Projection of a non-circular orbit relative to the local center of curvature to a circular
 443 orbit.
 444

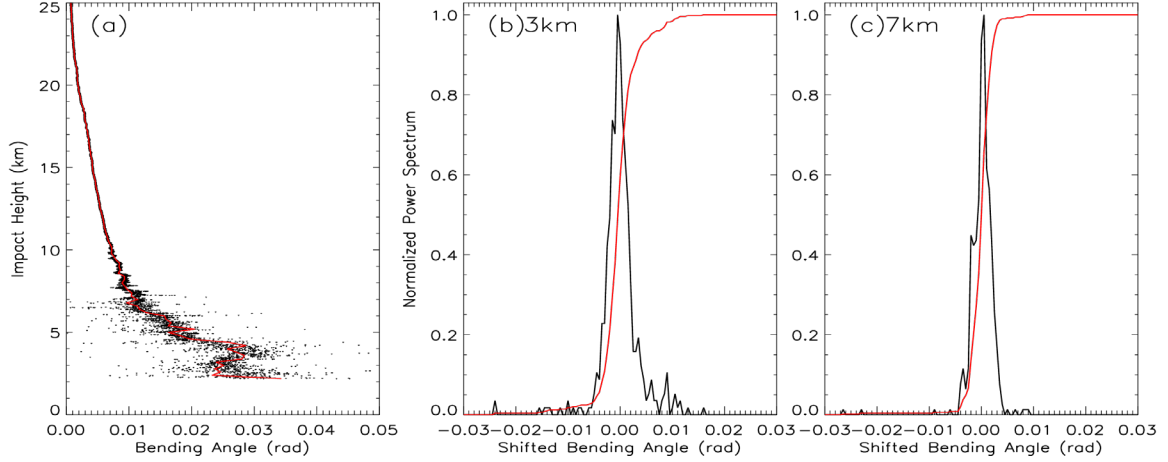
445
 446 After calculating bending angles for the L1 and L2 frequencies separately, the profiles are
 447 truncated using the FSI amplitude. This step is necessary because the FSI method produces
 448 bending angle and impact parameter pairs over an infinite range of impact parameters.
 449 Determining the lowest impact parameter and its corresponding bending angle is critical. In the
 450 current STAR FSI inversion approach, the pair with the lowest impact parameter and bending
 451 angle is identified based on the amplitude of the Fourier transform. The amplitude is first
 452 normalized using the signal's mean amplitude within the 10-50 km range. The lowest point is
 453 defined as the altitude at which the normalized amplitude drops below 0.35. This threshold is
 454 empirically determined based on extensive testing within the STAR FSI system. It represents
 455 an optimal balance between maximizing vertical penetration depth and minimizing noise-
 456 induced artifacts into the retrieved bending angle profile.
 457

458 3.2.4 Bending Angle Uncertainty Calculation

459
 460 The uncertainty in the bending angle is estimated using a sliding spectrogram with a 500 m
 461 window. First, a smoothed bending angle profile is generated to identify the central component.
 462 Then, the bending angle from the unsmoothed signal is calculated at 1 m impact height
 463 resolution. With each spectral window, deviations from the central component are used to
 464 construct a local power spectrum of the shifted bending angle, computed using a finite bending
 465 angle increment ($\delta\alpha = 0.0005$ rad). The shifted bending angle (α_s), is defined as the
 466 instantaneous bending angle minus the central component. The spectral width (Δs) is
 467 determined as the mean of the absolute value of the shifted bending angle weighted by the
 468 spectral power (ρ) of each component, as follows (which is similar to Liu et al. (2018)):
 469

$$470 \quad \Delta s = \sqrt{\frac{\sum_{i=1}^n \rho_i \alpha_s^2 \delta\alpha}{\sum_{i=1}^n \rho_i \delta\alpha}} \quad (17)$$

471
 472 Figure 3(a) presents a representative bending angle profile at 1 m resolution as a function of
 473 the impact height (black dots), along with its central component (red line). Figure 3(b) and 3(c)
 474 show the corresponding normalized power spectrum (black line) and accumulated power
 475 spectrum (red line) at impact heights of 3 km and 7 km, respectively. As illustrated, the spectral
 476 range at 3 km is broader than at 7 km, indicating greater atmospheric variability at lower
 477 altitudes. The bending angle uncertainty is quantified as half the spectral width, calculated
 478 using Eq. (17).
 479



480
481 Fig. 3: (a) Spectrogram of the RO signal, power spectrum at (b) 3 km, and (c) 7.5 km impact
482 heights.

483

484 3.3 Bending angle Inversion

485

486 3.3.1 Ionospheric Correction and Optimization

487

488 To remove first-order ionospheric effects, and as an approximation for the neutral atmosphere
489 bending angle, a linear combination of L1 and L2 bending angles ($\alpha_1(a)$ and $\alpha_2(a)$) is
490 computed (Vorob'ev and Krasil'nikova, 1994):

491

$$492 \alpha_{LC}(a) = \frac{\alpha_1(a)f_1^2 - \alpha_2(a)f_2^2}{f_1^2 - f_2^2} \quad (18)$$

493

494 where f_1 and f_2 are the RO frequencies.

495

496 This is followed by statistical optimization (Gorbunov, 2002c):

497

$$498 \alpha(a) = \alpha_{BG}(a) + \frac{\sigma^S}{\sigma^S + \sigma^N} (\alpha_{LC}(a) - \alpha_{BG}(a)) \quad (19)$$

499

500 where, σ^S and σ^N are the covariances of the neutral atmospheric signal and residual noise,
501 respectively, and $\alpha_{BG}(a)$ is the background bending angle from a climatological model (MSIS-
502 90 model).

503

504 Covariance matrices are estimated from the deviation ($\Delta\alpha$) of L1 and L2 bending angles from
505 the background model ($\alpha_{L1,L2} - \alpha_m$). For ionospheric signal and noise, deviations in the impact
506 heights (impact parameter minus local center of curvature) of 50-70 km are used; for neutral
507 atmospheric signal, the 12-35 km range is used. In the lower troposphere, near the surface,
508 where the L2 signals weaken, a constant correction is applied based on the lowest valid L2
509 altitude.

510

511 3.3.2 Abel Inversion

512

513 Refractivity is retrieved from ionosphere-corrected bending angles using the Abel transform
514 (Fjeldbo et al., 1971). The bending angle profile is extended up to 150 km using climatological
515 data (MSIS-90 model) to stabilize the upper boundary condition. Tangent point locations are

516 recovered by interpolating the occultation time and satellite positions. Since time information
517 is lost during the Fourier transform of the RO signal, the occultation time is reconstructed from
518 the bending angle-impact parameter profile and used to infer the latitude and longitude of each
519 tangent point.

520

521 **3.4 Quality control**

522

523 Due to the lack of effective internal quality control in the ROPP v10 package, we rely on
524 external quality control procedures to identify bad profiles. The fractional difference between
525 the observed (O) and simulated (B) bending angles, calculated from ERA5 forecast fields, is
526 used to assess the quality of the RO data at each altitude level:

527

$$528 \quad BA_{diff} = \frac{O-B}{B} \quad (20)$$

529

530 The annual mean standard deviation (σ_{year}) from 2020 is used as a benchmark. A profile is
531 flagged as ‘bad’ if the bending angle difference exceeds $7\sigma_{year}$ at any altitude level between 10
532 and 40 km, where RO data quality is highest and model-observation agreement is strongest. A
533 sensitivity study confirmed that using a 7σ year threshold provides an optimal balance between
534 data retention and data quality.

535

536 In addition, profiles are also flagged as ‘bad’ under any of the following conditions: (1) The
537 fractional BA difference exceeds $7\sigma_{year}$; (2) The top height of the profile is below 20 km; (3)
538 The bottom height is above 20 km; and (4) A negative bending angle is detected below 50 km.
539 The QC rejection rate for the ROMEX dataset depends on the mission. For example, the QC
540 pass rates are 85.7%, 94.8%, and 93.9% for COSMIC-2, Spire, and PlanetiQ, respectively.
541 These values are comparable to those from CDAAC-processed data: 87.6%, 95.7%, and 90.6%,
542 respectively. Note that quality control is not applied to PlanetiQ and Spire data processed by
543 EUMETSAT. To ensure a consistent comparison in this study (Section 4), we applied our
544 standard quality control procedure to the EUMETSAT dataset where quality control was
545 absent.

546

547 It is important to note that this quality control procedure applies only to bending angles within
548 a specific height range (10-40 km). In rare cases, even when the bending angle passes QC,
549 anomalies in refractivity or dry temperature may still occur due to limitations in the Abel
550 inversion. Future updates to the QC procedures will address such issues. This process ensures
551 that only high-quality profiles are retained as valid. An internal quality control system tailored
552 for near-real-time processing is under development; however, it was not incorporated into the
553 ROMEX data when that dataset was produced.

554

555 **4. Comparison Results**

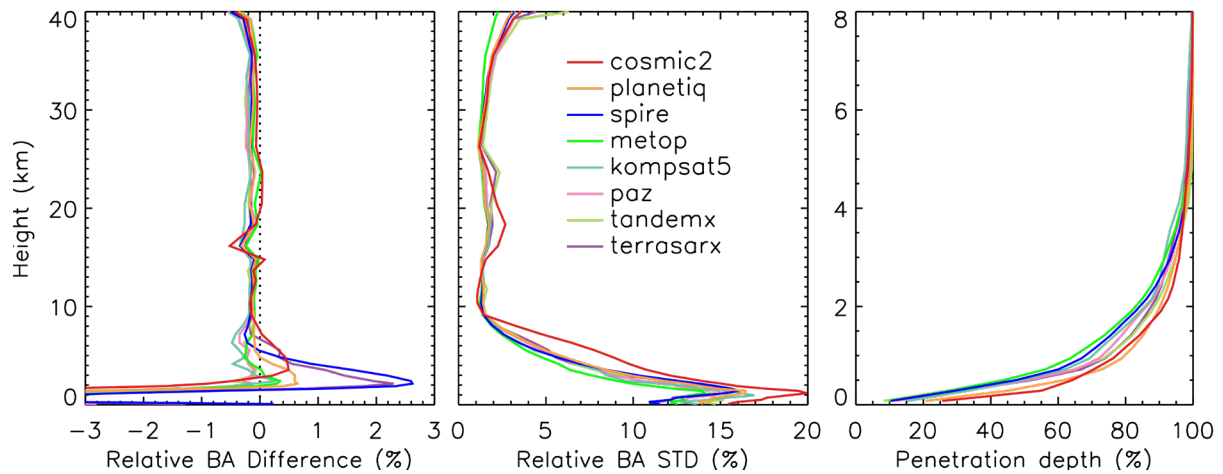
556

557 **4.1 Bending angle comparison with STAR RFSI, STAR ROPP, and EUMETSAT**

558

559 Figure 4 shows the height-dependent fractional bending angle differences between RO
560 observations and ERA5 background fields (O-B) for multiple satellite missions processed
561 using the RFSI algorithm during November 2022. The selected missions include COSMIC-2,
562 Spire, PlanetiQ, Metop-B, Metop-C, Komsat5, PAZ, TerraSAR-X, and TanDEM-X. The
563 comparison serves as a proxy for evaluating the quality and inter-mission consistency of RFSI-
564 processed RO data relative to a widely used global reanalysis.

565



566
 567 Fig. 4. Comparison of height-dependent fractional bending angle between RO observations
 568 and ERA5 simulations (O-B) among different RO missions. BA mean biases (left), standard
 569 deviations (middle) in terms of fractional BA difference (%), and (right) penetration depth
 570 below 8 km for RFSI over November 2022.

571
 572 In the middle and upper troposphere through the lower stratosphere (8-35 km), all missions
 573 exhibit excellent agreement with ERA5. Mean O-B differences are generally within $\pm 0.2\%$,
 574 and standard deviations remain below 3%, indicating high internal consistency among the RO
 575 datasets and strong alignment with ERA5 in this well-observed atmospheric region.

576
 577 In the lower troposphere (below 8 km), larger biases and variability are evident, especially near
 578 the surface. Spire and TerraSAR-X show mean biases up to 1-2% at 2 km, with standard
 579 deviations exceeding 10%. COMSIC-2 exhibits the highest variability in this region, with
 580 standard deviations approaching 20% at approximately 1 km. These discrepancies are likely
 581 attributed to increased atmospheric variability in the lower troposphere, limitations in signal
 582 tracking during multipath propagation at tropical/subtropical regions where high water vapor
 583 variability makes OL tracking difficult, and the sensitivity of bending angle retrievals to SNR
 584 cut-off thresholds. In contrast, PlanetiQ, Metop-B, and Metop-C demonstrate smaller near-
 585 surface biases (typically $< 0.5\%$) and reduced variability, suggesting robust signal tracking
 586 and/or more effective pre-processing of low-altitude data.

587
 588 Above 35 km, mean biases increase to approximately 0.6%, and standard deviations increase
 589 with height and can exceed 5% at 40 km. These deviations are primarily due to limitations in
 590 ionospheric correction at higher altitudes, where residual ionospheric effects are more
 591 challenging to remove completely. The ionospheric conditions during September-November
 592 2022 were generally moderate and typical for the ascending phase of Solar Cycle 25, but
 593 intermittently disturbed (including several geomagnetic storms and enhanced irregularities).
 594 They are not representative of worst-case conditions, but also not purely quiet-average; they
 595 are better described as moderately active with episodic disturbances.

596
 597 Among the evaluated missions, PlanetiQ consistently shows low mean biases and standard
 598 deviations across nearly the entire vertical range, indicating strong data stability and processing
 599 robustness. Metop-B and Metop-C also exhibit excellent performance, likely due to mature
 600 sensor platforms and the use of well-established pre-processing procedures in the ROPP
 601 system. Spire data, while reliable in the mid- to upper troposphere, shows elevated near-surface
 602 variability, likely due to its higher sensitivity to excess phase pre-processing (e.g., cycle-slip
 603 removal and parameter tuning).

604
605
606
607
608
609
610

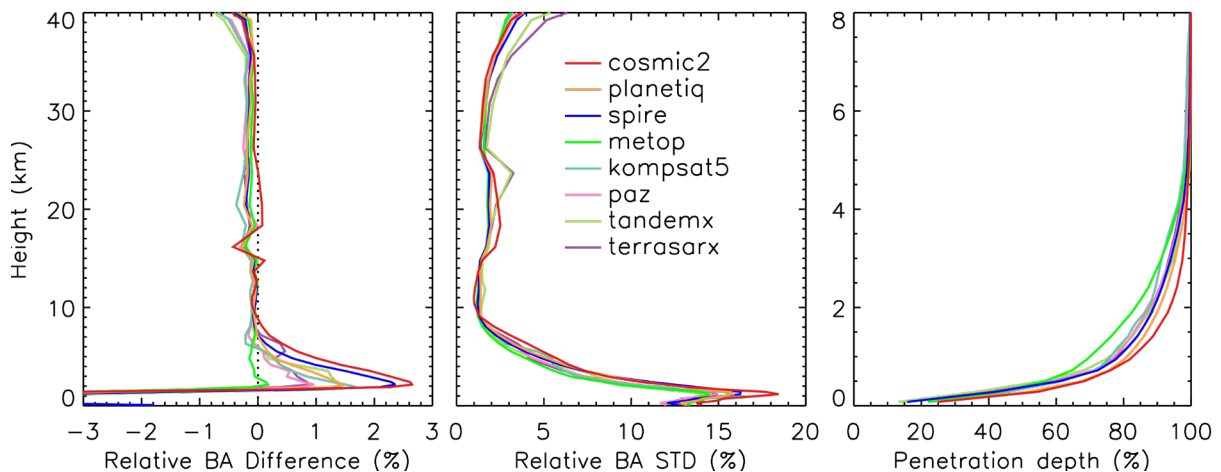
COSMIC-2 displays distinct behavior relative to other missions, with positive biases of 8-35 km and increased variability near the tropopause. These features are likely influenced by its low-inclination orbit and limited latitudinal coverage ($\pm 45^\circ$), which concentrates observations in tropical and subtropical regions with higher atmospheric variability. Similar features and their impact on data assimilation performance have been discussed in previous studies (Ho et al., 2023; Miller et al., 2025).

611
612
613
614
615
616
617
618
619
620
621
622
623
624

The penetration depth is defined as the minimum height above ground level where a valid (i.e., not filled or missing) bending angle or refractivity is obtained for a given RO event. Smaller penetration depths indicate that the RO signal reaches closer to the Earth's surface. Penetration depth depends on the signal cutoff criteria applied during processing (see Sections 3.1 and 3.2.3); therefore, comparisons among different missions should be made using the same processing center and algorithm. The right panel of Figure 4 shows the penetration depth profile below 8 km, expressed as the percentage of profiles reaching different altitudes relative to 8 km, for the FSI method. As discussed by Gorbunov et al. (2022a, 2022b), higher SNR generally improves tropospheric penetration. Consistent with Table 2, COSMIC-2 and PlanetiQ exhibit the greatest penetration depth among the missions. Most missions achieve more than 80% of occultations reaching 2 km or lower, and more than 50% reaching 1 km or lower. The penetration depths are noticeably higher for Metop-B and Metop-C (green line), while Spire, despite having the lowest SNR, achieves a slight better penetration than Metop.

625
626
627
628
629
630
631
632
633

Figure 5 shows O-B bending angle differences for the same missions and period, but with data processed using the STAR ROPP-CT2 method. The vertical structure of mean biases and variability is broadly similar to that in the RFSI results, reflecting consistent retrieval behavior between the two approaches. In the 8-35 km range, both methods yield small biases (within $\pm 0.2\%$) and standard deviations below 3%, confirming the reliability of both retrievals in the core atmospheric region. One exception is KOMPSAT-5, which shows a slight negative bias ($\sim -0.2\%$) between 17 and 23 km.



634
635
636

Fig. 5. Same as Fig. 4, but for RO data generated from the ROPP package using the CT2 method.

637
638
639
640
641

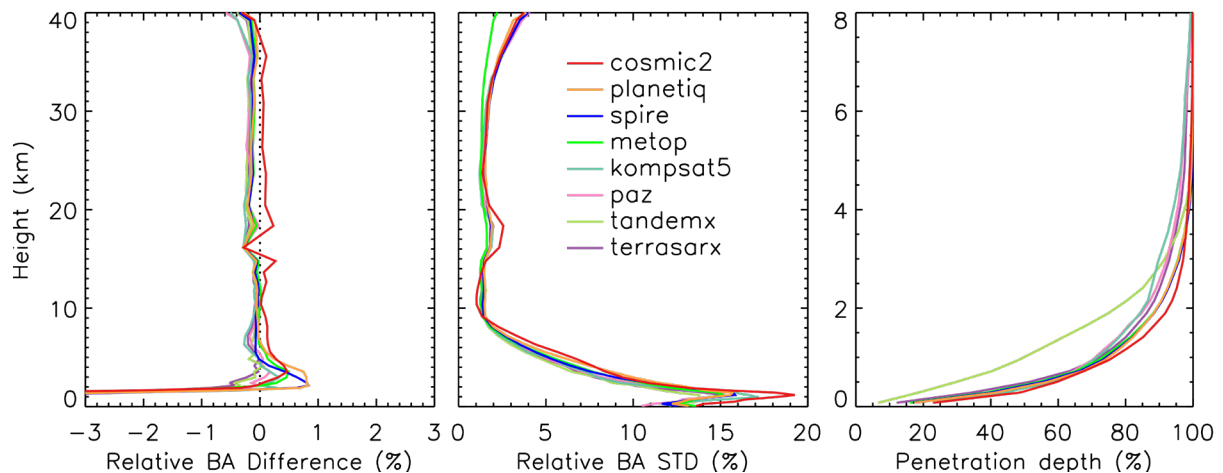
Standard deviations increase above 35 km and below 8 km in both datasets, highlighting common challenges in the upper and lower atmospheric regions, including multipath effects, signal noise, and uncertainty in ionospheric corrections. However, the CT2 retrievals generally exhibit larger near-surface biases than those of RFSI. For all missions except Metop-B and

642 Metop-C, the CT2-processed profiles exhibit biases of 1-2% near the surface, likely due to the
 643 more conservative use of signals and stronger smoothing.

644
 645 In contrast to Fig. 4, the penetration depth profiles among missions are much narrower below
 646 1 km, indicating that CT2 is less sensitive to SNR. Consistent with Fig. 4, COSMIC-2 and
 647 PlanetiQ show the deepest penetration depth among the missions. The penetration depths are
 648 noticeably higher for Metop-B and Metop-C than for Spire.

649
 650 Figure 6 displays ERA5 O-B differences for RO profiles processed by EUMETSAT, covering
 651 the same missions and period. The EUMETSAT-processed data (excluding COSMIC-2)
 652 utilized ROM SAF ROPP as the internal processing system, employing the CT2 method in the
 653 troposphere. Consistent with the other two datasets, EUMETSAT results show high
 654 consistency in the 8-35 km range, with mean biases within $\pm 0.2\%$ and standard deviations
 655 below 3%. COSMIC-2 again stands out, showing a positive bias of $\sim 0.2\%$, while most other
 656 missions exhibit slightly negative biases, suggesting a systematic offset in COSMIC-2 data
 657 relative to the ensemble.

658



659
 660 Fig. 6. Same as Fig. 4, but for RO data provided from EUMETSAT.
 661

662 In the lower troposphere, EUMETSAT retrievals exhibit the smallest mean biases ($<1\%$ at 2
 663 km) among the three datasets, suggesting more effective mitigation of noise and multipath
 664 effects near the surface. By comparison, RFSI-processed profiles for Spire and TerraSAR-X
 665 show near-surface biases of up to $\sim 2\%$, while STAR ROPP CT2 retrievals yield 1-2% biases
 666 for most missions. COSMIC-2 exhibits high variability below 8 km across all three datasets,
 667 although the CT2 method appears to reduce it slightly. Note that while STAR ROPP and
 668 EUMETSAT ROPP both use CT2 method in the troposphere, their specific configuration
 669 parameters may differ.

670
 671 Above 35 km, the bending angle uncertainty increases in all datasets. However, EUMETSAT
 672 results exhibit more uniform performance across missions, with mean biases generally below
 673 0.5% and smaller inter-mission variability. Metop-B and Metop-C show the lowest standard
 674 deviations across all datasets in this altitude range, indicating highly stable performance at high
 675 altitudes.

676
 677 The penetration depth from TanDEM-X is noticeably higher than that of other missions in the
 678 EUMETSAT-processed data. For Metop-B and Metop-C, penetration depths are substantially

679 improved compared with STAR RFSI and STAR ROPP CT2, and approach those of COSMIC-
680 2 and PlanetiQ below 1.5 km.

681

682 The comparatively shallower penetration depths observed for Metop (in Fig. 5) and TanDEM-
683 X (in Fig. 6) relative to missions like COSMIC-2 and PlanetiQ are linked to a combination of
684 mission-specific characteristics (specifically SNR) and the data truncation strategies employed
685 by the processing algorithm: 1) Impact of lower SNR: Penetration depth is fundamentally
686 dependent on the signal cutoff criteria applied during processing, and higher SNR is known to
687 improve tropospheric penetration. Metop-B/C and TanDEM-X exhibit lower mean SNRs (e.g.,
688 Metop-B GPS SNR is 730.2, TanDEM-X is 549.3) compared to the missions with the deepest
689 penetration (COSMIC-2 at 1295.1 and PlanetiQ at 1440.5). This lower SNR makes them more
690 susceptible to noise and multipath effects in the lower troposphere, leading to a shallower
691 signal cutoff. 2) Truncation strategy: The systematic signal truncation used in the STAR RFSI
692 method is based on SNR thresholds to prevent noise-contaminated signals from propagating.
693 For lower-SNR missions like Metop and TanDEM-X, these thresholds are reached at higher
694 altitudes, resulting in shallower penetration. 3) Processing algorithm variation: The choice of
695 processing algorithm also contributes to variation. The CT2 method, used in both ROPP
696 systems (STAR ROPP and ROM SAF ROPP), is less sensitive to SNR and resulted in generally
697 narrower penetration depth profiles below 1 km compared to RFSI. This is further reflected by
698 the fact that Metop-B/C penetration is substantially improved when processed by
699 EUMETSAT's CT2 compared to STAR's algorithms, suggesting differences in the specific
700 configuration parameters used by the processing centers.

701

702 Together, these intercomparisons highlight key trade-offs among the different retrieval
703 approaches. The RFSI method leverages the full frequency content of the RO signal, offering
704 enhanced sensitivity to fine-scale atmospheric features. However, it is also more sensitive to
705 noise, particularly near the surface. In contrast, the STAR ROPP CT2 method employs a
706 canonical transformation that simplifies retrieval but is more conservative in its use of signal
707 data, resulting in smoother profiles and slightly larger near-surface biases. EUMETSAT's
708 processing strikes a balance between these extremes, achieving consistent results across the
709 full vertical range while effectively suppressing noise in the lower troposphere and upper
710 stratosphere.

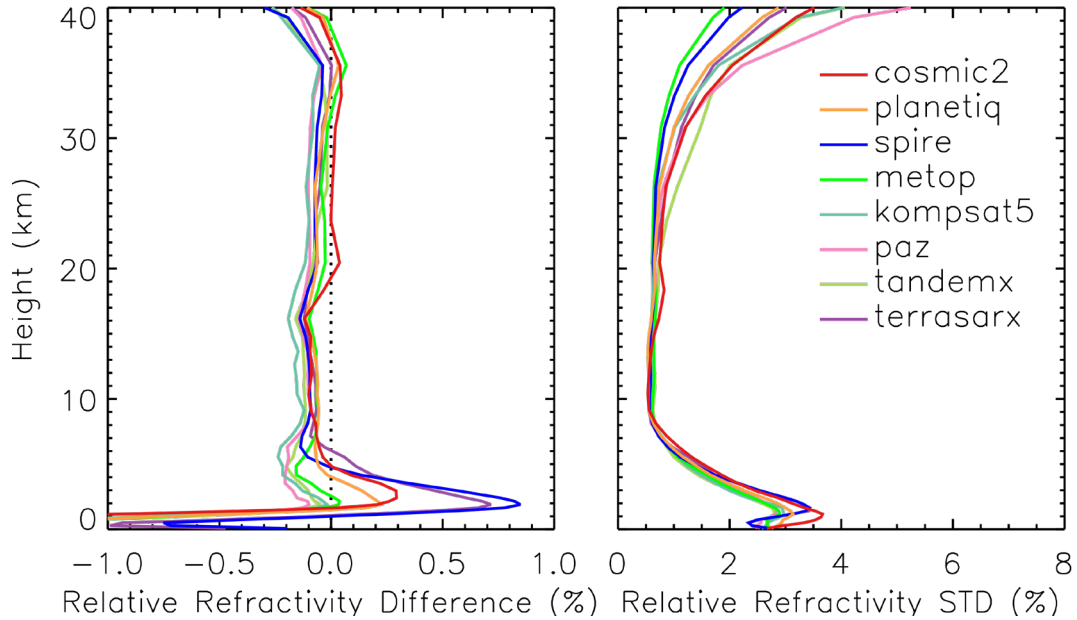
711

712 **4.2 Refractivity comparison with STAR RFSI, STAR ROPP, and EUMETSAT**

713

714 Figure 7 presents the fractional refractivity differences between RO observations processed
715 using the RFSI algorithm and ERA5 background fields for November 2022. The vertical
716 structures of refractivity O-B statistics largely mirror those of the bending angle differences
717 shown in Fig. 4, reflecting the propagation of bending angle quality into the refractivity
718 retrieval. In the well-constrained 8-30 km region, all missions show excellent agreement with
719 ERA5. Mean biases remain within $\pm 0.15\%$, and standard deviations are typically below 1%,
720 indicating that refractivity retrievals in this core region retain the stability and consistency of
721 the underlying bending angle data.

722



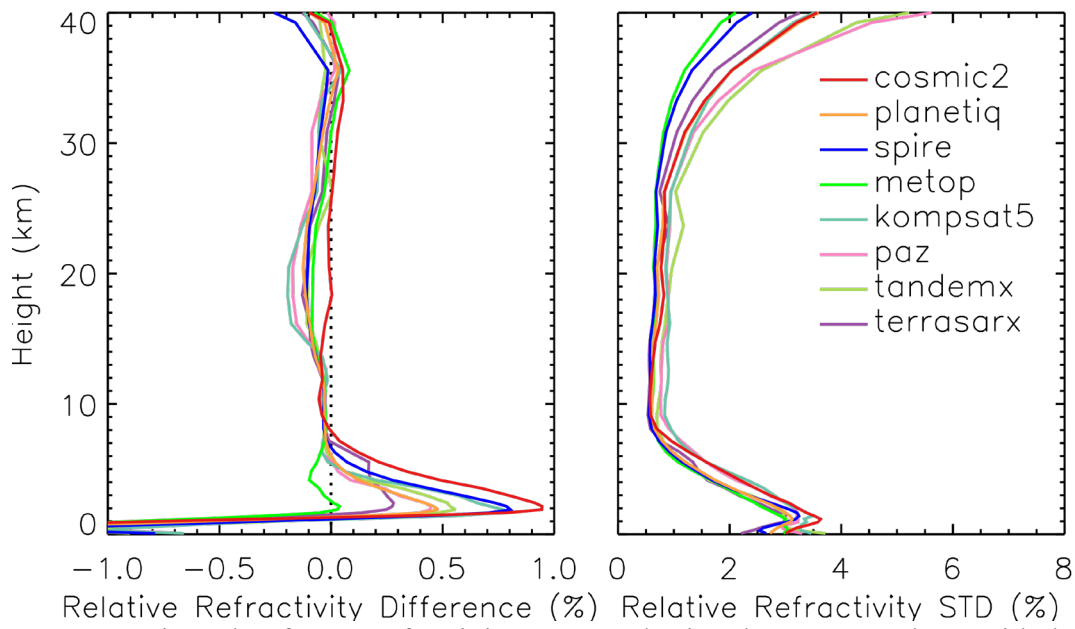
723 Fig. 7. Comparison of height-dependent fractional refractivity between RO observations and
 724 ERA5 simulations (O-B) among different RO missions. Refractivity mean biases (left) and
 725 standard deviations (right) in terms of fractional difference (%) for RFSI over November 2022.
 726

727
 728
 729 In the lower troposphere (below ~ 8 km), refractivity differences exhibit a significantly larger
 730 inter-mission spread, consistent with Fig. 4, although both biases and standard deviations are
 731 generally reduced. Spire and TerraSAR-X exhibit the most pronounced positive biases,
 732 reaching ~ 0.7 - 0.8% near 2 km, along with elevated standard deviations exceeding 3%.
 733 COSMIC-2 again exhibits high variability below 5 km, with standard deviations peaking at
 734 over 3.5% near 1 km. However, its mean refractivity bias remains relatively small compared
 735 to those from Spire or TerraSAR-X, suggesting increased random error rather than systematic
 736 offset.

737
 738 In the upper atmosphere (above ~ 35 km), where refractivity is less sensitive to the RO signal
 739 due to the exponential decrease in atmospheric density, the mean biases for all missions begin
 740 to increase negatively, reaching values of $\sim -0.2\%$ to -0.4% near 40 km. Standard deviations
 741 also rise, ranging from $\sim 2\%$ to 5%, consistent with the increased variability observed in the
 742 bending angle differences shown in Fig. 4. These errors are primarily attributed to residual
 743 ionospheric correction uncertainties and the influence of high-altitude extrapolation
 744 assumptions in the RFSI algorithm. The use of climatological models in the upper atmosphere
 745 also introduces additional variability, as refractivity becomes more sensitive to model
 746 inaccuracies in this region.

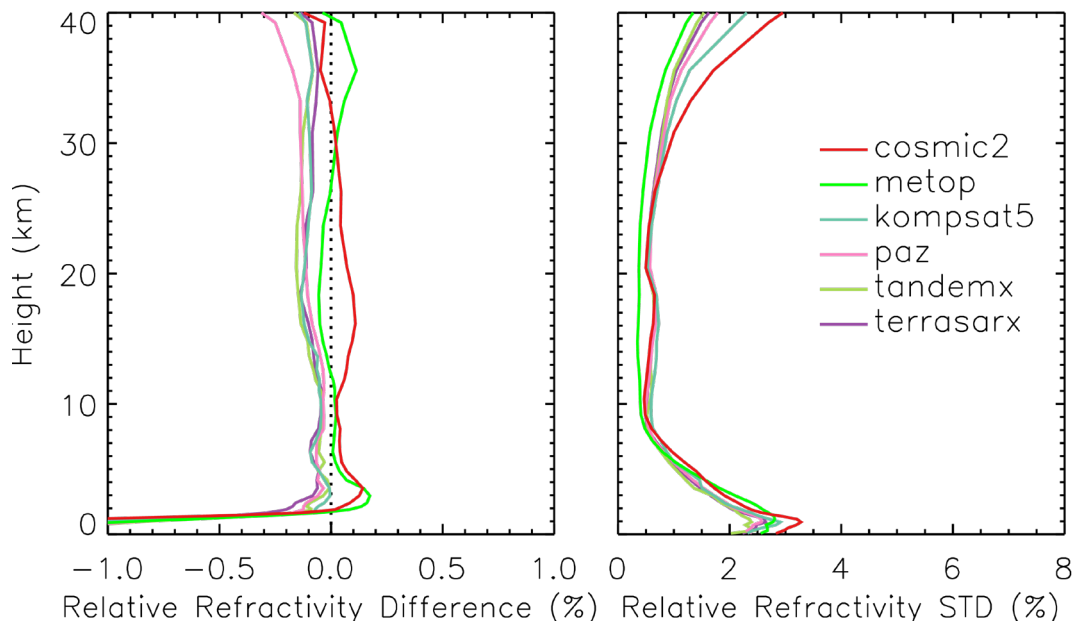
747
 748 Figure 8 shows the refractivity O-B differences derived from RO data processed with the ROPP
 749 CT2 method. Between 8 and 15 km, CT2 results exhibit improved inter-mission consistency
 750 in mean bias compared to RFSI, although the standard deviations are generally larger. In the
 751 lower troposphere (below ~ 8 km), CT2 retrievals produce larger positive biases, typically
 752 around 0.5-1% near 2 km (except for Metop-B, Metop-C, and TerraSAR-X), with the largest
 753 bias observed for COSMIC-2 ($\sim 1\%$). These biases are notably larger than those from RFSI,
 754 which remain below 0.3% for most missions, except for Spire and TerraSAR-X. Between 15-
 755 25 km, the CT2 results show a greater inter-mission spread in both mean bias and standard
 756 deviation compared to RFSI. Above 25 km, CT2 and RFSI show broadly similar behavior,

757 with rising uncertainty consistent with bending angle trends. Note that both RFSI and CT2 used
 758 geometric optics method above 25 km.
 759



760 Relative Refractivity Difference (%) Relative Refractivity STD (%)
 761 Fig. 8. Same as Fig. 7, but for RO refractivity processed using the ROPP package with the CT2
 762 method.

763
 764 Figure 9 presents the refractivity O-B differences from the EUMETSAT dataset. Note that
 765 refractivity profiles are not available for PlanetiQ and Spire in this dataset. Similar to bending
 766 angle results, COSMIC-2 exhibits a distinct positive bias in the 4-30 km region, along with a
 767 notably larger inter-missions spread in the 8-40 km range compared to CT2 (Fig. 8) and RFSI
 768 (Fig. 7) results. In contrast, in the lower troposphere (below ~8 km), the EUMETSAT retrievals
 769 show the smallest near-surface mean biases, generally within $\pm 0.2\%$ above 2.5 km, and the
 770 lowest standard deviation across all available missions. These results suggest that the
 771 refractivity data from EUMETSAT are particularly effective at mitigating noise and multipath
 772 effects near the surface.
 773



774 Relative Refractivity Difference (%) Relative Refractivity STD (%)

775 Fig. 9. Same as Fig. 7, but for RO data provided from EUMETSAT. Note that refractivity data
776 is not available in the EUMETSAT dataset for PlanetiQ and Spire.

777

778 Taken together, the comparisons between Figs. 4 and 7, Figs. 5 and 8, and Figs. 6 and 9 reveal
779 that many mission-specific features observed in bending angle retrievals persist in the
780 refractivity domain. This reinforces the importance of bending angle quality, particularly near
781 the surface and in the upper atmosphere, for achieving accurate refractivity retrievals. The
782 heightened sensitivity of refractivity to small-scale errors at the profile boundaries also
783 underscores the need for robust quality control, optimized signal tracking, and careful
784 algorithm design in future RO missions and processing systems.

785

786 **4.3 Structural Uncertainty among Different Processing Methods**

787

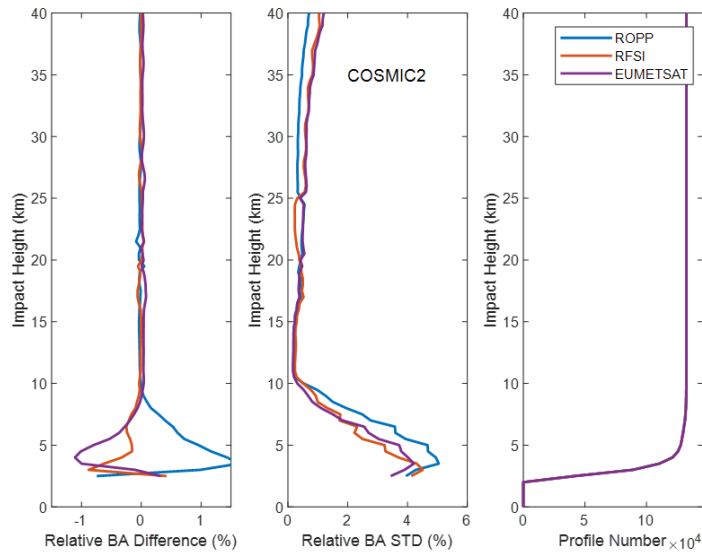
788 Figures 10-14 illustrate the structural bending angle uncertainty associated with the ROPP
789 (CT2), RFSI, and EUMETSAT processing algorithms for five representative GNSS RO
790 missions: COSMIC-2, Spire, PlanetiQ, Metop-B, and Metop-C. For each mission, the figure
791 shows the height-dependent relative mean differences and standard deviations of bending
792 angles with respect to the three-dataset mean, along with the number of common profiles
793 processed for each algorithm.

794

795 Several important structural differences emerge from these comparisons:

796

797 For COSMIC-2 (Fig. 10), the three processing methods demonstrate strong consistency in the
798 middle and upper troposphere and stratosphere (above ~ 10 km), where both the relative
799 differences and standard deviations of bending angles remain below approximately 0.1% and
800 1%, respectively, indicating minimal structural uncertainty. Below 10 km, method-dependent
801 differences become more pronounced. The largest deviations are observed near the surface,
802 with relative differences of approximately 1.5% for ROPP, -1.0% for EUMETSAT, and -0.5%
803 for RFSI. Additionally, the ROPP algorithm exhibits higher bending angle standard deviations
804 in the lowest 10 km, indicating greater sensitivity to retrieval ambiguities under conditions of
805 multipath propagation. In contrast, above 25 km, ROPP shows slightly lower standard
806 deviations than RFSI and EUMETSAT. Despite these lower-tropospheric differences, the
807 overall structural agreement among the three COSMIC-2 processing methods is robust.
808 Although the number of available profiles (right panel) decreases significantly near the surface,
809 sufficient observations are present throughout the vertical domain to enable meaningful
810 statistical comparisons.

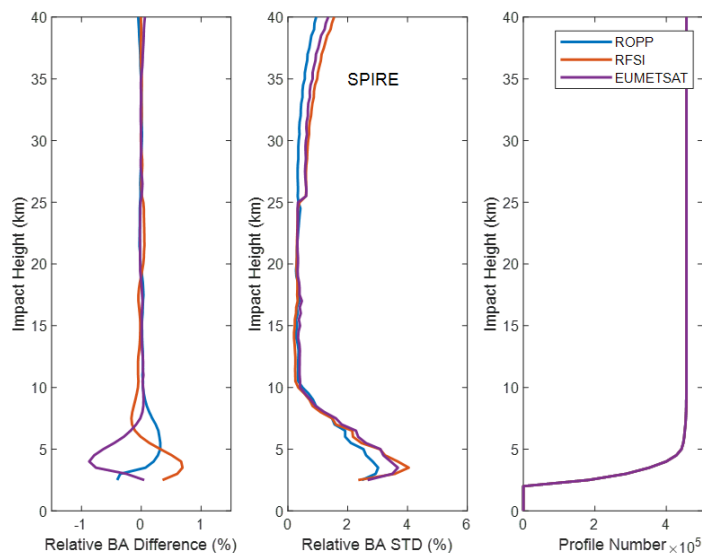


811

812 Fig. 10. Structural bending angle uncertainty among different processing methods for
 813 COSMIC-2. Note that the bending angle profiles from the EUMETSAT dataset are processed
 814 by the UCAR CDAAC using the phase-matching method.

815

816 For Spire (Fig. 11), a similar pattern of agreement is observed. Above approximately 10 km,
 817 the relative bending angle differences across the three methods are generally within $\pm 0.1\%$,
 818 and the standard deviations remain below 1% up to approximately 35 km, indicating good
 819 consistency in the upper atmosphere. However, RFSI exhibits a distinct pattern in the 8-25 km
 820 range, with a relative positive difference in the 19-25 km region and a negative difference in
 821 the 8-19 km region, compared to the nearly identical ROPP and EUMETSAT solutions. As
 822 with COSMIC-2, larger discrepancies emerge below 10 km. Notably, the ROPP and RFSI
 823 solutions show small positive differences near the surface (up to $\sim 0.7\%$ and $\sim 0.3\%$,
 824 respectively), whereas the EUMETSAT solution exhibits a negative deviation of up to -1.0% .
 825 The bending angle standard deviations in the lower troposphere are higher for RFSI and
 826 EUMETSAT, reaching $\sim 4\%$, while ROPP shows slightly lower variability (below 3%) near
 827 the surface. Above 25 km, ROPP again yields lower standard deviations compared to the other
 828 two methods, consistent with the COSMIC-2 results.

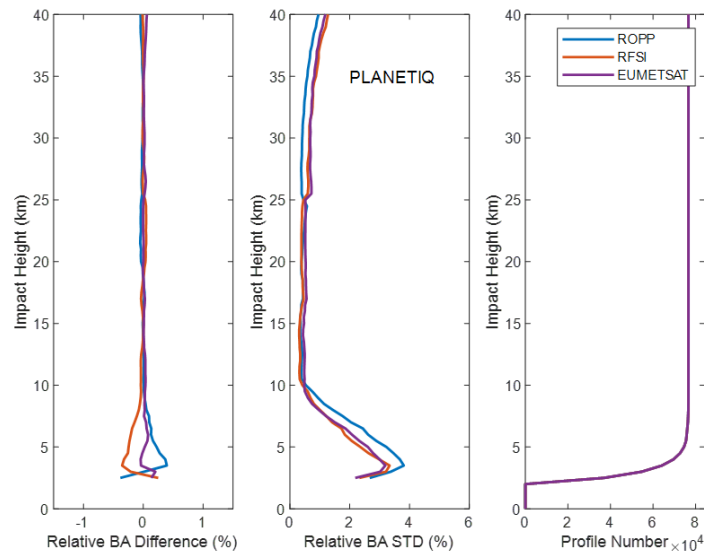


829

830 Fig. 11. Same as Fig. 10, but for Spire.

831
 832
 833
 834
 835
 836
 837
 838
 839
 840
 841
 842
 843
 844
 845
 846

For PlanetiQ (Fig. 12), a higher level of consistency is observed among the three processing methods across the vertical profile compared to those from COSMIC-2 and Spire. Above ~ 10 km, the solutions are nearly identical, except for a slight positive deviation in the 19–25 km region from the RFSI solution. Relative bending angle differences remain within $\pm 0.05\%$, and standard deviations are below 1% up to ~ 38 km, indicating excellent agreement in the middle and upper atmosphere. Below 10 km, small but systematic differences become evident. The ROPP solution shows a modest positive bias, peaking at approximately $+0.4\%$ near a 3 km impact height, while the RFSI solution exhibits a slight negative bias of similar magnitude. The EUMETSAT data remain close to zero throughout this region. As with COSMIC-2, the standard deviations increase toward the surface, with ROPP exhibiting greater variability below 10 km than RFSI and EUMETSAT. However, for PlanetiQ, the overall variability is lower, reaching a standard deviation of $\sim 3\%$ near the surface. This improved consistency suggests enhanced robustness in PlanetiQ’s onboard processing, a more stable tracking geometry and antenna design, and higher SNR, which may reduce sensitivity to differences among retrieval algorithms.



847
 848

Fig. 12. Same as Fig. 10, but for PlanetiQ.

849

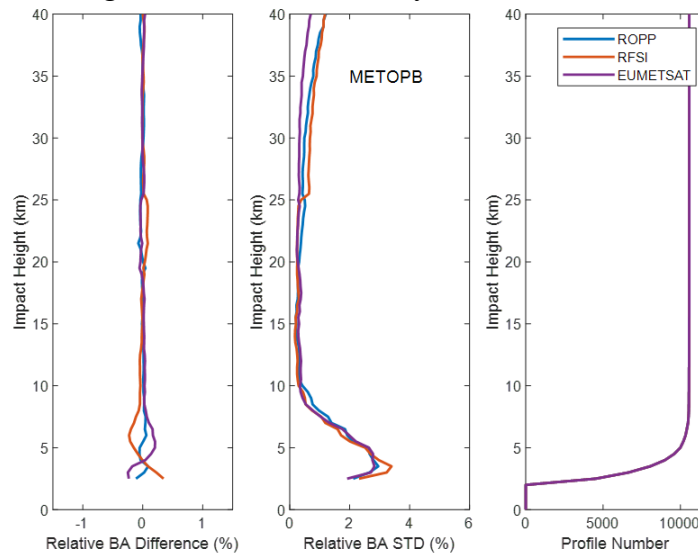
850
 851
 852
 853
 854
 855
 856
 857

Metop-B (Fig. 13) and Metop-C (Fig. 14), both long-operational polar-orbiting satellites with mature and well-characterized instrumentation, exhibit nearly identical inter-method structural uncertainties. For brevity, the discussion here focuses on Metop-B. Below an impact height of ~ 8 km, the standard deviation profiles from all three algorithms converge closely, indicating similar variability near the surface. Relative bending angle differences show a maximum positive deviation of approximately $+0.2\%$ for the EUMETSAT solution and a negative deviation of about -0.2% for RFSI near 5 km.

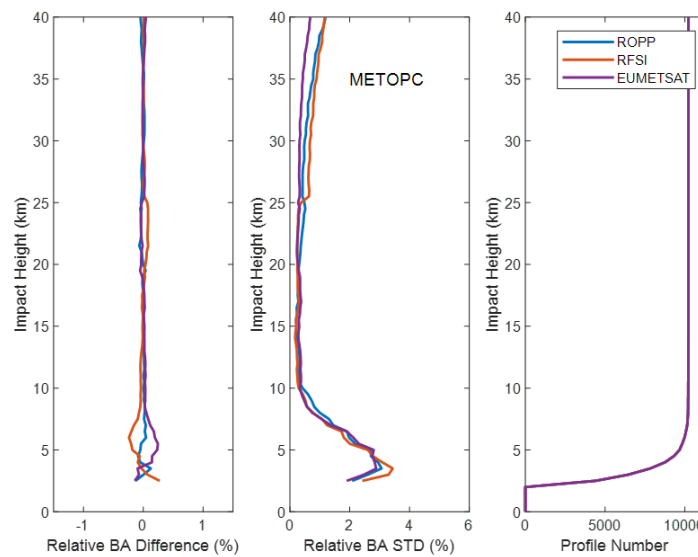
858
 859
 860
 861
 862
 863
 864
 865

In contrast, the ROPP solution remains close to zero. A slight negative bias is also observed in the RFSI solution below ~ 13 km ($\sim -0.1\%$). In the upper stratosphere, above 25 km, a clear separation in variability emerges: RFSI exhibits the largest standard deviations, followed by ROPP, with EUMETSAT showing the lowest variability. This divergence in STD differences near 25 km for Metop-B/C, compared to COSMIC-2, PlanetiQ, and Spire, suggests that the upper-atmospheric retrievals for Metop-B/C are more sensitive to processing methodology. This is supported by the data showing that in the upper stratosphere (above 25 km), the EUMETSAT algorithm exhibits the lowest variability. Given that Metop-B/C are EUMETSAT

866 missions and their data are routinely processed by EUMETSAT, this superior performance
 867 suggests that the EUMETSAT processing methodology is likely fine-tuned and highly stable
 868 for their mature sensor platforms, enabling effective mitigation of noise and uncertainties at
 869 high altitudes, and resulting in the lowest variability observed across all datasets.



870
 871 Fig. 13. Same as Fig. 10, but for Metop-B.
 872



873
 874 Fig. 14. Same as Fig. 10, but for Metop-C.
 875

876 Except for COSMIC-2, RFSI shows a small positive bias (<0.1%) at 20–25 km for Spire,
 877 PlanetiQ, and Metop-B/C relative to STAR ROPP and EUMETSAT. Possible causes include
 878 spectral windowing and filtering choices, as RFSI applies a sliding polynomial filter below 25
 879 km and an optimal estimation filter above 25 km, potentially introducing systematic offsets.
 880 Degraded L2 signals and reduced GNSS SNR at ~20-25 km further amplify noise, and because
 881 FSI is more noise-sensitive than geometric optics or canonical transform methods, incomplete
 882 noise suppression may yield small positive biases. The exact causes are under active
 883 investigation to further mitigate this effect.

884
 885 These results highlight that structural uncertainty is both algorithm- and mission-dependent,
 886 influenced by signal quality, onboard processing, antenna design, and orbit characteristics. The

887 findings highlight the crucial role of processing methodology in ensuring consistency and
888 accuracy in retrieving RO bending angle data, particularly when data from diverse missions
889 are used in operational weather forecasting systems. Future efforts in GNSS RO should focus
890 on developing harmonized processing standards and conducting inter-comparison studies to
891 quantify and mitigate structural uncertainty in bending angle datasets.

892

893 **5. Discussions and Summary**

894

895 This study presents the first comprehensive cross-mission intercomparison of the STAR-
896 developed Full Spectrum Inversion algorithm with the community-standard ROPP CT2 and
897 EUMETSAT dataset within the framework of ROMEX. Using bending angle and refractivity
898 profiles from key GNSS RO missions (e.g., COSMIC-2, Spire, PlanetiQ, Metop-B/C) during
899 the ROMEX period (September–November 2022), we assessed inter-algorithm consistency
900 against ERA5 reanalysis and structural uncertainty against the three-dataset mean.

901

902 A significant finding is the excellent agreement among all three processing methods in the
903 middle and upper troposphere and lower stratosphere (8–35 km). In this region, the mean
904 bending angle differences remained within $\pm 0.2\%$ and the standard deviations were below 3%,
905 demonstrating the maturity and robust internal coherence of RO observations across diverse
906 missions. Similarly, refractivity retrievals in this core region exhibited high stability, with mean
907 biases within $\pm 0.15\%$ and standard deviations typically below 1%.

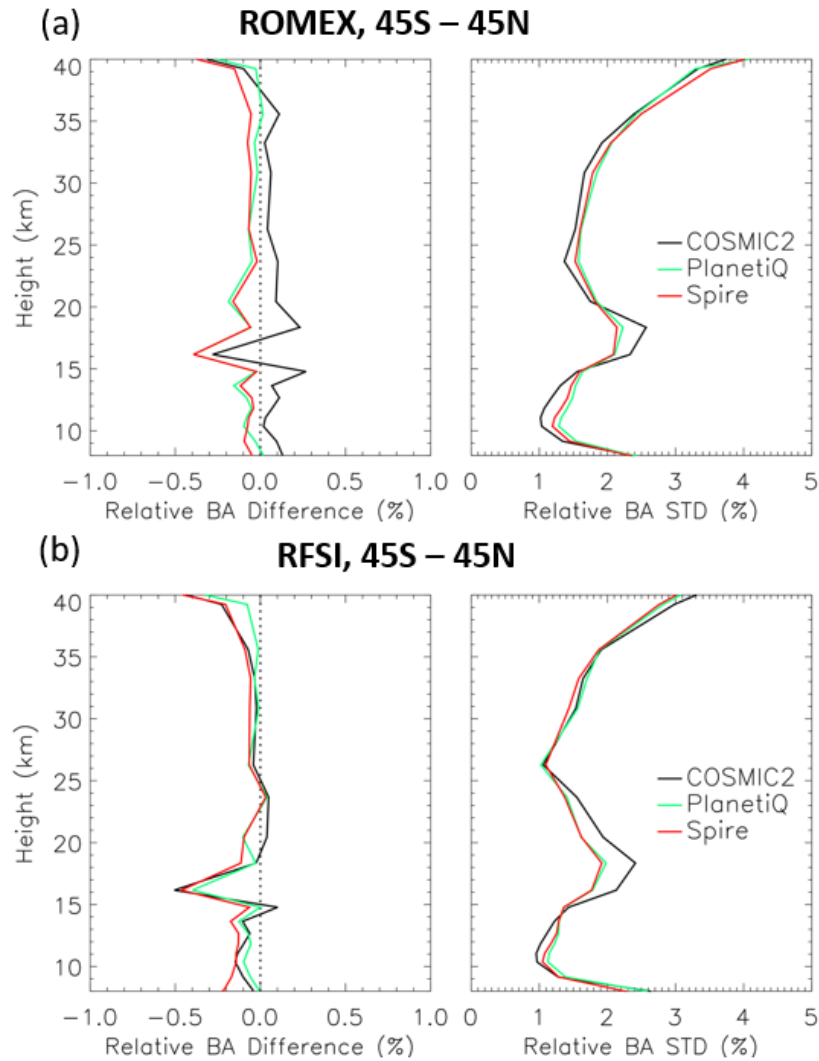
908

909 Anthes et al. (2025) reported that the UCAR-processed COSMIC-2 bending angles included
910 in ROMEX exhibit a positive bias of approximately 0.1–0.15% relative to ERA5 in the lower
911 stratosphere, larger than the biases seen for Spire and other ROMEX datasets. Similar lower-
912 stratospheric positive biases for UCAR COSMIC-2 have also been documented by Ho et al.
913 (2024, 2025). This difference is predominantly a representativeness effect associated with
914 orbit-dependent sampling over a non-spherical Earth (the azimuth effect), rather than a true
915 systematic bias, and therefore does not significantly impact data assimilation. The remaining
916 small component (less than 0.05%) is attributed to the sideways displacement of the occultation
917 plane and can be mitigated by impact height correction during RO processing (Anthes et al.,
918 2025). Figure 15 provides a zoomed-in comparison of the height-dependent fractional O–B
919 bending-angle differences for the COSMIC-2, Spire, and PlanetiQ missions, between the
920 EUMETSAT/UCAR processing and the STAR RFSI processing. In Fig. 15a, the COSMIC-2
921 data are from UCAR, while the Spire and PlanetiQ datasets are processed by EUMETSAT; in
922 Fig. 15b, all three missions are processed consistently by STAR RFSI.

923

924 While the UCAR-provided COSMIC-2 ROMEX datasets show a small positive O-B bias
925 compared to EUMETSAT-processed Spire and PlanetiQ data in the lower stratosphere (Fig.
926 15a), the STAR RFSI-processed COSMIC-2 bending angles exhibit improved consistency with
927 the Spire and PlanetiQ results (Fig. 15b). One contributing factor may be the treatment of
928 horizontal tangent-point sliding within the RFSI framework. While a consistent occultation
929 point definition is applied across missions in this study, differences in occultation point
930 definitions (or georeferencing) among processing centers can affect the magnitude of the
931 sliding-related correction. As noted in Anthes et al. (2025), UCAR defines the occultation point
932 as the location where the L1 excess phase exceeds 500 m, typically in the lower troposphere.
933 In contrast, RFSI defines it as the location where the straight-line tangent altitude equals zero,
934 typically in the upper troposphere-lower stratosphere (UTLS). This sideways sliding effect can
935 introduce a positive bias in COSMIC-2 bending angles of up to $\sim 0.05\%$. The underlying cause

936 of the subtle differences in the lower-stratospheric O–B bending-angle among the processing
 937 centers (STAR, EUMETSAT, UCAR) will be examined further in future work.



938 Fig. 15. Zoomed-in height-dependent fractional bending-angle differences (O–B) between RO
 939 observations and ERA5 simulations are shown for COSMIC-2, Spire, and PlanetiQ. Panels (a)
 940 and (b) display the mean bending-angle biases (left) and standard deviations (right) for RO
 941 data processed by EUMETSAT and by STAR RFSI, respectively.
 942

943
 944 Conversely, larger discrepancies and heightened variability emerged in the lower troposphere
 945 (below ~8 km) and upper atmosphere (above ~35 km). These regions are challenged by
 946 multipath effects, increased tracking noise, and varying SNR. The FSI method, designed to
 947 resolve fine-scale atmospheric structures by leveraging full-spectrum signal information,
 948 demonstrated improved sensitivity in the lower atmosphere (Adhikari et al., 2021), particularly
 949 for missions such as PlanetiQ and Metop-B/C. However, it also showed increased variability
 950 and greater dependence on SNR cut-off and quality control thresholds, as seen with Spire and
 951 TerraSAR-X near the surface. In contrast, the CT2 method, while generally yielding smoother
 952 profiles with reduced noise, sometimes showed larger near-surface biases (e.g., CT2 for
 953 COSMIC-2 and Spire), suggesting a more conservative approach that might underestimate
 954 bending in complex conditions. EUMETSAT's dataset, in particular, achieved the smallest
 955 near-surface bending angle and refractivity biases across missions, indicating effective
 956 mitigation of noise and multipath.

957

958 A crucial finding of this study is that structural uncertainty depends on both the processing
959 algorithm and the satellite mission. A greater inter-method spread was observed across all
960 missions below 8 km, likely due to their distinct approaches to handling multipath, noise, and
961 signal truncation. This structural uncertainty complicates the consistent use of multi-mission
962 RO data. For instance, COSMIC-2 data processed by ROPP CT2 showed higher near-surface
963 variability than those processed by RFSI and EUMETSAT. In contrast, missions like Metop-
964 B/C exhibited stronger consistency across all three methods, while PlanetiQ demonstrated the
965 highest inter-method consistency throughout the profile. These mission-specific patterns,
966 clearly illustrated in Figs. 10-14, underscore the critical need to characterize and account for
967 algorithmic effects when assimilating multi-mission RO data into operational weather
968 forecasting systems. The explicit comparison of the total O-B standard deviation (Figs. 4-6)
969 with the structural uncertainty (Figs. 10-14) quantifies the contribution of retrieval algorithm
970 differences to the total error budget, demonstrating that structural differences account for
971 approximately one-fourth of the total O-B standard deviation over all the altitudes, providing
972 a critical metric for interpreting ROMEX forecast impact studies and refining GNSS RO data
973 assimilation systems.

974
975 The ROMEX results unequivocally highlight the importance of quantifying algorithm-related
976 structural uncertainty for data assimilation applications. To ensure a consistent and optimal
977 representation of RO data in numerical weather prediction systems, it may be necessary to
978 harmonize retrieval strategies across different processing centers or to apply mission- and
979 algorithm-specific bias corrections.

980
981 The successful integration of STAR's FSI algorithm into ROPP version 10.0 represents a
982 significant advancement, providing users with a robust and flexible alternative to existing
983 algorithms. This enhancement facilitates consistent RO data processing across both
984 government-funded and commercial missions, offering customizable settings to meet specific
985 scientific and operational requirements.

986
987 In summary, this study demonstrates the critical influence of algorithm choice, particularly in
988 the lower troposphere; confirms strong consistency among processors in the mid-to-upper
989 atmosphere; identifies distinct mission-dependent structural uncertainties; and recommends
990 applying bias correction or ensemble strategies to improve data assimilation. The findings
991 strongly support continued efforts to harmonize across agencies through collaborative
992 initiatives, such as ROMEX. As the volume and diversity of GNSS RO data continue to
993 expand, these insights underscore the paramount need for robust algorithm development,
994 thorough uncertainty quantification, and coordinated processing strategies to fully leverage RO
995 observations and advance weather forecasting and climate monitoring capabilities.

996
997 **Code/Data availability.** The ROMEX data processed by EUMETSAT are available free of
998 charge through ROM SAF, subject to the ROMEX terms and conditions. Further information
999 is available at <https://irowg.org/ro-modeling-experiment-romex/> (last access: 27 May 2026).
1000 The ROMEX data processed by NOAA/STAR are available from STAR under the ROMEX
1001 terms and conditions. ERA5 data are available from the ECMWF data catalogue at
1002 <https://www.ecmwf.int/en/forecasts/datasets/browse-reanalysis-datasets> (last access: 27 May
1003 2026).

1004
1005 **Author contribution.** YC developed the RO processing system and designed the research
1006 plan, supervised the study, and prepared the manuscript. XZ conducted the data processing and
1007 prepared the figures and analysis. XJ contributed to the preparation of the data analysis and

1008 figures. SH provided overall scientific guidance throughout the project. XS and TL led the
1009 theoretical development and conducted testing to improve the results. All co-authors
1010 contributed to the interpretation of the results and to the writing and revision of the manuscript.

1011

1012 **Competing interests.** The contact author has declared that none of the authors has any
1013 competing interests.

1014

1015 **Disclaimer. Publisher’s note:** Copernicus Publications remains neutral with regard to
1016 jurisdictional claims made in the text, published maps, institutional affiliations, or any other
1017 geographical representation in this paper. While Copernicus Publications makes every effort
1018 to include appropriate place names, the final responsibility lies with the authors. Views
1019 expressed in the text are those of the authors and do not necessarily reflect the views of the
1020 publisher.

1021

1022 **Special issue statement.** This article is part of the special issue “The Radio Occultation
1023 Modeling EXperiment (ROMEX): observational quality, processing, and numerical weather
1024 prediction (NWP) applications”. It is not associated with a conference.

1025

1026 **Acknowledgments**

1027 This research received no external funding and was supported by the NOAA Center for
1028 Satellite Applications and Research (STAR). We thank the ROMEX coordination team and the
1029 ROM SAF for facilitating access to the processed datasets. This work was further supported
1030 by the NOAA/NESDIS/STAR Product Development Readiness and Applications (PDRA)
1031 fund and by NOAA grants NA19NES4320002 and NA24NESX432C0001 (Cooperative
1032 Institute for Satellite Earth System Studies-CISESS) at the University of Maryland/ESSIC. The
1033 authors also thank Dr. Loknath Adhikari for his contributions to the development of the FSI
1034 algorithm, Josep Aparicio and two anonymous reviewers for their constructive suggestions,
1035 which have helped improve the quality and clarity of this manuscript. The scientific results and
1036 conclusions, as well as any views or opinions expressed herein, are those of the author(s) and
1037 do not necessarily reflect those of NOAA or the Department of Commerce.

1038

1039 **References**

1040 Adhikari, A., Xie, F., and Haase, J. S.: Application of the full spectrum inversion algorithm to
1041 simulated airborne GPS radio occultation signals, *Atmos. Meas. Tech.*, 9, 5077–5086,
1042 <https://doi.org/10.5194/amt-9-5077-2016>, 2016.

1043

1044 Adhikari, A., Ho, S.-P., and Zhou, X.: Inverting COSMIC-2 phase data to bending angle and
1045 refractivity using the Full Spectrum Inversion method, *Remote Sens.*, 13, 1793,
1046 <https://doi.org/10.3390/rs13091793>, 2021.

1047

1048 Anthes, R. A.: Exploring Earth’s atmosphere with radio occultation: Contributions to weather,
1049 climate, and space weather, *Atmos. Meas. Tech.*, 4, 1077–1103, <https://doi.org/10.5194/amt-4-1077-2011>, 2011.

1051

1052 Anthes, R. A., Bernhardt, P. A., Chen, Y., Cucurull, L., Dymond, K. F., Ector, D., Healy, S.
1053 B., Ho, S.-P., Hunt, D. C., Kuo, Y.-H., and others: The COSMIC/FORMOSAT-3 Mission:
1054 Early Results, *Bull. Amer. Meteor. Soc.*, 89, 313–334, <https://doi.org/10.1175/BAMS-89-3-313>, 2008.

1056

1057 Anthes, R. A., Marquardt, C., Ruston, B., and Shao, H.: Radio Occultation Modeling
1058 Experiment (ROMEX): Determining the impact of radio occultation observations on numerical
1059 weather prediction, *Bull. Amer. Meteor. Soc.*, 105, E1552–E1568,
1060 <https://doi.org/10.1175/BAMS-D-23-0326.1>, 2024.

1061
1062 Anthes, R., Sjoberg, J., Starr, J., and Zeng, Z.: Evaluation of biases and uncertainties in
1063 ROMEX radio occultation observations, *Atmos. Meas. Tech.*, 18, 6997-7019,
1064 <https://doi.org/10.5194/amt-18-6997-2025>, 2025.

1065
1066 Born, M. and Wolf, E.: *Principles of Optics*, Cambridge University Press, New York, 1999.

1067
1068 Chen, Y., Zhou, X., Ho, S.-P., Shao, X., and Liu, T.-C.: Comparison of Radio Occultation
1069 Bending Angle and Refractivity Processed by Different Inversion Algorithms from Multi-RO
1070 Missions, in: *IGARSS 2024 IEEE Int. Geosci. Remote Sens. Symp.*, Athens, Greece, 2024,
1071 8904–8907, <https://doi.org/10.1109/IGARSS53475.2024.10641034>, 2024.

1072
1073 Cucurull, L., Derber, J. C., Treadon, R., and Purser, R. J.: Assimilation of global positioning
1074 system radio occultation observations into NCEP’s Global Data Assimilation System, *Mon.*
1075 *Weather Rev.*, 135, 3174–3193, <https://doi.org/10.1175/MWR3461.1>, 2007.

1076
1077 Fjeldbo, G. F., Kliore, A. J., and Eshelman, V. R.: The neutral atmosphere of Venus as studied
1078 with the Mariner V radio occultation experiments, *J. Astro.*, 76, 123–140, 1971. Gorbunov, M.,
1079 Irisov, V., and Rocken, C.: The Influence of the Signal-to-Noise Ratio upon Radio Occultation
1080 Retrievals, *Remote Sens.*, 14, 2742, <https://doi.org/10.3390/rs14122742>, 2022a.

1081
1082 Gorbunov, M., Irisov, V., and Rocken, C.: Noise Floor and Signal-to-Noise Ratio of Radio
1083 Occultation Observations: A Cross-Mission Statistical Comparison, *Remote Sens.*, 14, 691,
1084 <https://doi.org/10.3390/rs14030691>, 2022b.

1085
1086 Gorbunov, M. E.: Radioholographic analysis of radio occultation data in multipath zones,
1087 *Radio Sci.*, 37, 1008, <https://doi.org/10.1029/2000RS002577>, 2002a.

1088
1089 Gorbunov, M. E.: Canonical transform method for processing radio occultation data in the
1090 lower troposphere, *Radio Sci.*, 37, 1076, <https://doi.org/10.1029/2000RS002592>, 2002b.

1091
1092 Gorbunov, M. E.: Ionospheric correction and statistical optimization of radio occultation data,
1093 *Radio Sci.*, 37, <https://doi.org/10.1029/2000RS002370>, 2002c.

1094
1095 Gorbunov, M. E., Lauritsen, K. B., Rhodin, A., Tomassini, M., and Kornblueh, L.: Analysis of
1096 the CHAMP experimental data on radio-occultation sounding of the Earth’s atmosphere, *Izv.*
1097 *Atmos. Ocean. Phys.*, 41, 798–813, 2005.

1098
1099 Hajj, G. A., Kursinski, E. R., Romans, L. J., Bertiger, W. I., and Leroy, S. S.: A technical
1100 description of atmospheric sounding by GPS occultation, *J. Atmos. Sol.-Terr. Phys.*, 64, 451–
1101 469, [https://doi.org/10.1016/S1364-6826\(01\)00114-6](https://doi.org/10.1016/S1364-6826(01)00114-6), 2002.

1102
1103 Healy, S. B.: Forecast impact experiment with a constellation of GPS radio occultation
1104 receivers, *Atmos. Sci. Lett.*, 9, 111–118, <https://doi.org/10.1002/asl.169>, 2008.

1105

1106 Hersbach, H., Bell, B., Berrisford, P., Biavati, G., Horányi, A., Muñoz Sabater, J., Nicolas, J.,
1107 Peubey, C., Radu, R., Rozum, I., Schepers, D., Simmons, A., Soci, C., Dee, D., and Thépaut,
1108 J.-N.: ERA5 hourly data on pressure levels from 1940 to present, Copernicus Climate Change
1109 Service (C3S) Climate Data Store (CDS) [data set], <https://doi.org/10.24381/cds.bd0915c6>,
1110 accessed: 27 May 2026.

1111

1112 Hedin, A. E., Extension of the MSIS thermosphere model into the middle and lower
1113 atmosphere, *J. Geophys. Res.*, 96, 1159–1172, 1991.

1114

1115 Liu, H., Kuo, Y.-H., Sokolovskiy, S., Zou, X., Zeng, Z., Hsiao, L.-F., and Ruston, B.: A quality
1116 control procedure based on bending angle measurement uncertainty for radio occultation data
1117 assimilation in the tropical lower troposphere, *J. Atmos. Oceanic Tech.*, 35(10), 2117-2131,
1118 2018, doi: 10.1075/JTECHD-17.0224.1.

1119

1120 Ho, S.-P., Anthes, R. A., Ao, C. O., Healy, S., Horányi, A., Hunt, D., Mannucci, A. J.,
1121 Pedatella, N., Randel, W. J., and Simmons, A.: The COSMIC/FORMOSAT-3 Radio
1122 Occultation Mission after 12 Years: Accomplishments, Remaining Challenges, and Potential
1123 Impacts of COSMIC-2, *Bull. Amer. Meteor. Soc.*, 101, E1107–E1136,
1124 <https://doi.org/10.1175/BAMS-D-19-0027.1>, 2020.

1125

1126 Ho, S.-P., Hunt, D., Steiner, A. K., Mannucci, A. J., Kirchengast, G., Gleisner, H., Heise, S.,
1127 von Engeln, A., Marquardt, C., Sokolovskiy, S., Schreiner, W., Scherllin-Pirscher, B., Ao, C.,
1128 Wickert, J., Syndergaard, S., Lauritsen, K. B., Leroy, S., Kursinski, E. R., Kuo, Y.-H.,
1129 Foelsche, U., Schmidt, T., and Gorbunov, M.: Reproducibility of GPS radio occultation data
1130 for climate monitoring: Profile-to-profile inter-comparison of CHAMP climate records 2002
1131 to 2008 from six data centers, *J. Geophys. Res.*, 117, D18111,
1132 <https://doi.org/10.1029/2012JD017665>, 2012.

1133

1134 Ho, S.-P., Zhou, X., Shao, X., Chen, Y., Jing, X., and Miller, W.: Using the Commercial GNSS
1135 RO Spire Data in the Neutral Atmosphere for Climate and Weather Prediction Studies, *Remote
1136 Sens.*, 15, 4836, <https://doi.org/10.3390/rs15194836>, 2023.

1137

1138 Ho, S.-P., Shao, X., Chen, Y., Zhou, J., Gu, G., Miller, W., and Jing, X.: Lessons Learned from
1139 the Preparation and Evaluation of Multiple GNSS RO Data for the ROMEX from
1140 NOAA/STAR. Presentation at the COSMIC/JCSDA Workshop and IROWG-10, Boulder,
1141 Colorado, 12-18 September 2024. Available at: [https://www.cosmic.ucar.edu/events/cosmic-
1142 jcsda-workshop-irowg-10/agenda](https://www.cosmic.ucar.edu/events/cosmic-jcsda-workshop-irowg-10/agenda), 2024.

1143

1144 Ho, S.-P., Shao, X., Chen, Y., Zhou, J., and Miller, W.: Advances in ROMEX data processing
1145 and evaluation: Lessons from NOAA STAR. Presentation at the 2nd ROMEX Workshop,
1146 February 27, 2025, at EUMETSAT, Darmstadt, Germany. Available at
1147 <https://www.eventsforce.net/romex2025>, 2025.

1148

1149 Jensen, A. S., Lohmann, M., Benzon, H.-H., and Nielsen, A. S.: Full spectrum inversion of
1150 radio occultation signals, *Radio Sci.*, 38, 1040, <https://doi.org/10.1029/2002RS002763>, 2003.

1151

1152 Jensen, A. S., Lohmann, M., Nielsen, A. S., and Benzon, H.-H.: Geometrical optics phase
1153 matching of radio occultation signals, *Radio Sci.*, 39, RS3009,
1154 <https://doi.org/10.1029/2003RS002899>, 2004.

1155

1156 Kursinski, E. R., Hajj, G. A., Schofield, J. T., Linfield, R. P., and Hardy, K. R.: Observing
1157 Earth's atmosphere with radio occultation measurements using the Global Positioning System,
1158 *J. Geophys. Res.*, 102, 23429–23465, <https://doi.org/10.1029/97JD01569>, 1997.
1159

1160 Luzum, B. and Petit, G.: The IERS conventions (2010): Reference systems and new models,
1161 *Proc. Int. Astron. Union*, 10, 227–228, 2012.
1162

1163 Miller, W., Chen, Y., Ho, S.-P., and Shao, X.: Exploring the Value of Spire GNSS Radio
1164 Occultation Bending Angle Assimilation for Improving HWRP Model Forecasts of Atlantic
1165 Hurricane Intensity, *Weather and Forecasting*, 40 (6), 809-827, [https://doi.org/10.1175/waf-d-](https://doi.org/10.1175/waf-d-24-0092.1)
1166 [24-0092.1](https://doi.org/10.1175/waf-d-24-0092.1), 2025.
1167

1168 Paoletta, S., et al. (2025). Assessment of operational non-time-critical Sentinel-6A Michael
1169 Freilich radio occultation data: insights into tropospheric GNSS signal cut-off strategies and
1170 processor improvements. *Atmos. Meas. Tech.*, 18, 2825–2845. [https://doi.org/10.5194/amt-18-](https://doi.org/10.5194/amt-18-2825-2025)
1171 [2825-2025](https://doi.org/10.5194/amt-18-2825-2025)
1172

1173 Petit, G. and Luzum, B. (Eds.): IERS Technical Note No. 36, IERS, Frankfurt am Main, 2010,
1174 available at: <https://apps.dtic.mil/sti/citations/ADA535671> (last access: 27 May 2026).
1175

1176 Rocken, C., Anthes, R., Exner, M., Hunt, D., Sokolovskiy, S., Ware, R., Gorbunov, M.,
1177 Schreiner, W., Feng, D., Herman, B., Kuo, Y.-H., and Zou, X.: Analysis and validation of
1178 GPS/MET data in the neutral atmosphere, *J. Geophys. Res.-Atmos.*, 102, 29849–29866,
1179 <https://doi.org/10.1029/97JD02400>, 1997.
1180

1181 Schreiner, W. S., Weiss, J. P., Anthes, R. A., Braun, J., Chu, V., Fong, J., Hunt, D., Kuo, Y.-
1182 H., Meehan, T., Serafino, W., Sjoberg, J., Sokolovskiy, S., Talaat, E., Wee, T. K., and Zeng,
1183 Z.: COSMIC-2 radio occultation constellation: First results, *Geophys. Res. Lett.*, 47,
1184 e2019GL086841, <https://doi.org/10.1029/2019GL086841>, 2020.
1185

1186 Shao, H., and Folsche, U.: ROMEX: Status and First Lessons Learned, Presentation at IROWG
1187 CGMS-52 Plenary, 2024, Washington, DC, USA. Available at [https://irowg.org/wpcms/wp-](https://irowg.org/wpcms/wp-content/uploads/2025/04/CGMS-52-IROWG-WP-03.pdf)
1188 [content/uploads/2025/04/CGMS-52-IROWG-WP-03.pdf](https://irowg.org/wpcms/wp-content/uploads/2025/04/CGMS-52-IROWG-WP-03.pdf), 2024.
1189

1190 Sokolovskiy, S., Rocken, C., Schreiner, W., Hunt, D., and Johnson, J.: Postprocessing of L1
1191 GPS radio occultation signals recorded in open-loop mode, *Radio Sci.*, 44, RS2002,
1192 <https://doi.org/10.1029/2008RS003907>, 2009.
1193

1194 Sokolovskiy, S., Rocken, C., Schreiner, W., and Hunt, D.: On the uncertainty of radio
1195 occultation inversions in the lower troposphere, *J. Geophys. Res.*, 115, D22111,
1196 <https://doi.org/10.1029/2010JD014058>, 2010.
1197

1198 Steiner, A. K., Lackner, B. C., Pirscher, B., Hegerl, G. C., and Foelsche, U.: The contribution
1199 of radio occultation to the assessment of tropospheric temperature trends, *J. Climate*, 24, 4936–
1200 4950, <https://doi.org/10.1175/2011JCLI3982.1>, 2011.
1201

1202 Steiner, A. K., Ladstädter, F., Ao, C. O., Gleisner, H., Ho, S.-P., Hunt, D., Schmidt, T.,
1203 Foelsche, U., Kirchengast, G., Kuo, Y.-H., and others: Consistency and structural uncertainty
1204 of multi-mission GPS radio occultation records, *Atmos. Meas. Tech.*, 13, 2547–2575,
1205 <https://doi.org/10.5194/amt-13-2547-2020>, 2020.

1206
1207 The Radio Occultation Processing Package (ROPP) Pre-processor Module User Guide, version
1208 10.0, ROM SAF Consortium, Ref: SAF/ROM/METO/UG/ROPP/004, 30 September 2020.
1209
1210 Vorob'ev, V. V. and Krasil'nikova, T. G., Estimation of the accuracy of the atmospheric
1211 refractive index recovery from Doppler shift measurements at frequencies used in the
1212 NAVSTAR system, *USSR Phys. Atmos. Ocean, Engl. Transl.*, 29, 602–609, 1994.